REPORT DOCUMENTATION PAGE

AFRL-SR-BL-TR-01-

0494

1. AGENCY USE ONLY *(Leave blank)*	2. REPORT DATE	3. REPORT TITLE AND
		15 Mar 98 to 14 Nov 00 Final

4. TITLE AND SUBTITLE
Periodic Lattices of Interacting Self-Assembled Quantum Dots

5. FUNDING NUMBERS
61102F
2305/EX

6. AUTHOR(S)
Dr. Speck

7. PERFORMING ORGANIZATION NAME(S) AND ADDRESS(ES)
University of California
Cheadle Hall
Santa Barbara, CA 93106-2050

8. PERFORMING ORGANIZATION REPORT NUMBER

9. SPONSORING/MONITORING AGENCY NAME(S) AND ADDRESS(ES)
AFOSR/NE
801 North Randolph Street Rm 732
Arlington, VA 22203-1977

10. SPONSORING/MONITORING AGENCY REPORT NUMBER

F49620-98-1-0367

11. SUPPLEMENTARY NOTES

AIR FORCE OFFICE OF SCIENTIFIC RESEARCH (AFOSR)
NOTICE OF TRANSMITTAL DTIC. THIS TECHNICAL REPORT
HAS BEEN REVIEWED AND IS APPROVED FOR PUBLIC
LAW AFR 190-12. DISTRIBUTION IS UNLIMITED.

12a. DISTRIBUTION AVAILABILITY STATEMENT
APPROVAL FOR PUBLIC RELEASED; DISTRIBUTION UNLIMITED

12b. DISTRIBUTION CODE

13. ABSTRACT *(Maximum 200 words)*

Overall, in this program, we developed high quality 2D and 3D periodic quantum dot lattices that show strong photoluminescence. In the initial stages of the program, we worked on QD growth on a periodic stressor lattice formed by ordered subsurface dislocations. The dislocation grid was formed by twist bonding.

14. SUBJECT TERMS

15. NUMBER OF PAGES

16. PRICE CODE

17. SECURITY CLASSIFICATION OF REPORT	18. SECURITY CLASSIFICATION OF THIS PAGE	19. SECURITY CLASSIFICATION OF ABSTRACT	20. LIMITATION OF ABSTRACT
UNCLASSIFIED	UNCLASSIFIED	UNCLASSIFIED	UL

Standard Form 298 (Rev. 2-89) (EG)
Prescribed by ANSI Std. 239.18
Designed using Perform Pro, WHS/DIOR, Oct 94

Air Force Contract
Final Report

Periodic Lattices of Interacting Self-Assembled Quantum Dots

Air Force Award Number F49620-98-1-0367

PIs:
James S. Speck
Pierre M. Petroff
Glenn E. Beltz

Materials Department
University of California
Santa Barbara, CA 93106

1

Objective:

In this program we developed a novel approach to achieve, in a relatively simple manner, ordered self-assembled quantum dot (SAQD) arrays with long range ordering and controlled three-dimensional periodicity. The ordering of the array relies on the *nucleation of the SAQDs on a periodic lattice of surface specific sites*.

Program Summary and Highlights:

Year 1   Demonstration of periodic stressor lattice based on a dislocation cross-grid.
Optimization of re-growth on twist-bonded layers
Completion of mechanics of twist-bonded layers
Decision to abandon twist-bonding
Development of holographic lithography for periodic mesa lattice
Demonstration of quantum dot (QD) growth on the holographically-defined lattices
Demonstration of strong photoluminescence from capped QDs on mesa lattice

Year 2   Addition of a stressor layer to the mesa lattice
Demonstration of 2D periodic QD arrays
Demonstration of strong PL from periodic QD lattices

Year 3   Demonstration of 3D periodic QD arrays
Completion of comprehensive mechanics studies of subsurface QDs
Preliminary demonstration of GaN QDs on partially relaxed AlN buffers.

Synopsis:

Overall, in this program, we developed high quality 2D and 3D periodic quantum dot lattices that show strong photoluminescence. In the initial stages of the program, we worked on QD growth on a periodic stressor lattice formed by ordered subsurface dislocations. The dislocation grid was formed by twist bonding. However, this approach failed because the buffer layer regrowth thickness was too large to a sustain a sufficient strain modulation. We then developed holographic lithography and formed a mesa lattice. In the absence of a stressor, the QDs would typically nucleate in the mesa valleys, not the mesa tops. With the addition of a stressor layer, we demonstrated high quality QD growth on the mesa tops and subsequent stacking of the dots. This work was guided by solid mechanics calculations, careful buffer layer growth studies
In the second year of the program, we have successfully developed a periodic subsurface stressor lattice that has enabled the growth of *ordered* two-dimensional InAs quantum dot arrays. The periodicity of these arrays is controlled by holographic lithography.

2

The full details of this work is found in the Appendices I at the end of this report and two attached papers.

Personnel Supported:
Overall, this program supported activities of three faculty, one visiting scientist, one post-doctoral researcher, and three graduate students.

Faculty:
James S. Speck – Materials Dept.
Pierre Petroff – Materials Dept. and ECE Dept.
Glenn Beltz – Mechanical Engineering Dept.

Visiting Faculty:
Alexei Romanov – Materials Dept. (from Ioffe Institute, St. Petersburg, Russia)

Post-Doctoral Reserachers
Hao Lee – Materials Dept.

Graduate Students
Bill Fischer – Mechanical Engineering Dept. – M.S., 2000
Jo Anna Johnson – Materials Dept., M.S., 2000
Jay Brown – Materials Dept., in progress

Publications (attached):
"Lateral ordering of quantum dots by periodic subsurface stressors"
A. E. Romanov, P. M. Petroff, and J. S. Speck, *Appl. Phys. Lett.*, **74**, 2280 (1998).

"Controlled ordering and positioning of InAs self-assembled quantum dots"
H. Lee, J.A. Johnson, J.S. Speck, and P.M. Petroff, *J. Vac. Sci. Tech. B* **18**, 2193 (2000)

"Approaches for Determination of the Elastic Fields of Quantum Dots in Subsurface Layers"
A.E. Romanov, G.E. Beltz, W.T. Fischer, P.M. Petroff and J.S. Speck, *J. Appl. Phys.* **89**, 4523 (2001).

"Strain Engineered Self-Assembled Semiconductor Quantum Dot Lattices"
H. Lee, J.A. Johnson, M.Y. He, J.S. Speck, and P.M. Petroff, *Appl. Phys. Lett.* **78**, 105 (2001).

Presentations:
Gordon Conference on Nanoclusters. Connecticut College. July 1999.
Invited talk

International Conference on Modulated Semiconductor Structures. Fukuoka, Japan. July 1999.
Oral presentation

International Workshop on Nanostructures. Venice, Italy. April 1999.
Invited talk

Conference on *Physics and Chemistry of Semconductor Interfaces* (PCSI), Salt Lake City, January 2000.

Electronic Materials Conference (EMC), Denver, June 2000

Quantum Dots 2000, Munich, Germany, July 2000, *Invited talk*

Lateral ordering of quantum dots by periodic subsurface stressors

A. E. Romanov,[a] P. M. Petroff, and J. S. Speck[b]

Materials Department, University of California, Santa Barbara, California 93106

We investigate the possibility of using subsurface dislocation arrays as a tool for controlling the nucleation of self-assembled quantum dots (SAQDs). A quantitative model predicts that periodic nonuniform elastic fields on the surface induced by dislocations may control the lateral ordering SAQDs. The effect of dislocations is shown to be comparable to the interaction between buried and surface dots which leads to vertical dot stacking. The periodic subsurface dislocation arrays necessary for dot ordering can be produced by twist wafer bonding and backside substrate removal. © *1999 American Institute of Physics.* [S0003-6951(99)00916-X]

By providing a way for investigating three-dimensional confinement of carriers and excitons, self-assembled quantum dots (SAQDs) have attracted substantial recent attention.[1] Size distribution and dot density are among the most important issues for SAQD device application (e.g., quantum dot lasers). SAQD formation is often observed in mismatched epitaxy.[2] For example, the Stranski–Krastanow (SK) growth of InAs (or $In_xGa_{1-x}As$) on GaAs first involves the growth of a ~1–2 monolayer thick "wetting layer" followed by coherent island formation.[2,3] The SAQDs may be buried by growth of the same material as the underlying substrate. Subsequent growth of the strained composition on the buried dot template has been shown to lead to vertical stacking of dots provided that the thickness of the intervening layer (the "spacer layer") is on the order or thinner than the lateral dimension of individual dots.[4,5] Despite the possibility for vertical ordering of dots, the SAQDs do not show lateral order. Theoretical modeling suggests that lateral ordering of SAQDs will lead to both improved size uniformity and the possibility of long range correlation in the electronic structure of the dot assembly.[6,7]

The aim of the present work is in developing the technique for controlling the dot nucleation and growth conditions at the surface. Since typical dots have mesoscopic sizes (diameter $d \approx 50–200$ Å, height $c \approx 30–60$ Å, and dot spacing $l = 150–1000$ Å),[1–5] their behavior can be most effectively influenced on the mesoscopic level. Thus, it is necessary to develop a technique that can produce well-controlled preferred surface sites for dot nucleation with mesoscale periodicity. Below we will demonstrate that the interfacial dislocation arrays, such as may be achieved in wafer bonding and backside substrate removal, provide a reasonable and practically important example of two-dimensional periodic subsurface stressors that could be used for that nucleation of a periodic lattice of islands.

The role of uniform strains and stresses in the processes of island nucleation and evolution has been addressed in a number of theoretical and experimental studies.[8–11] It has been previously shown that surface roughness is an effective mechanism for strain energy release in lattice mismatched epitaxial layers.[9] Freund has shown that strain affects surface diffusion and further demonstrated that interfacial misfit dislocations could be responsible for surface roughness of semicoherent films.[11,12] Recently, similar ideas were applied to the analysis of dot stacking.[4,5,7,13] Due to the lattice mismatch (for example for InAs dots in a GaAs matrix have a misfit $f = 0.067$), buried dots become strong sources of elastic strains and stresses. Calculations of the elastic fields have been carried out under different assumptions and by using various techniques.[14,15] It was assumed that new quantum dots nucleate at the positions that minimize the total elastic energy of the system of buried and surface dots.[7,13] An alternative approach by Xie *et al.*[4] (but similar to the approach of Jonsdottir and Freund[12]) treated adatom migration along the surface strained by a buried dot.

To analyze the influence of different types of stressors on the evolution of quantum dot ensembles, we use the elastic energy density e at the surface as a measure of the preference of new quantum dot formation at the surface or in the subsurface layer (a similar criteria was used by Rouvimov *et al.*[5]). We calculate this elastic energy density for a cross grid of screw dislocations, as well as for subsurface dilatated inclusions. In the case of dislocations, we derive the analytic strain field for a cross grid of dislocations based on the known solution for a single subsurface screw dislocation.[16] We approximate the buried quantum dots as ellipsoidal subsurface inclusions, for which the analytical solution for the elastic fields has been previously developed.[17]

The geometry of a subsurface cross grid of screw dislocations is shown in Fig. 1(a). One family of screw dislocations has lines parallel to the z axis, and the other family has lines parallel to the y axis; the yz plane coincides with the free surface where the quantum dots will form. The spacing between dislocations in each array is l, and they are placed at distance h from the free surface. The dislocation Burgers vectors are $b_s\mathbf{e}_z$ or $b_s\mathbf{e}_y$, where b_s is the magnitude of the dislocation Burgers vector, and $\mathbf{e}_z$ and $\mathbf{e}_y$ are unit vectors along the corresponding coordinate axes. It is well known that such a planar dislocation cross grid represents a model for a small angle twist boundary.[16] The angle of misorientation ω is related to parameters of the array by the relation $\omega = b_s/l$, where $\omega \ll 1$.

[a]Permanent address: A. F. Ioffe Physico-Technical Institute, 194021 St. Petersburg, Russia.
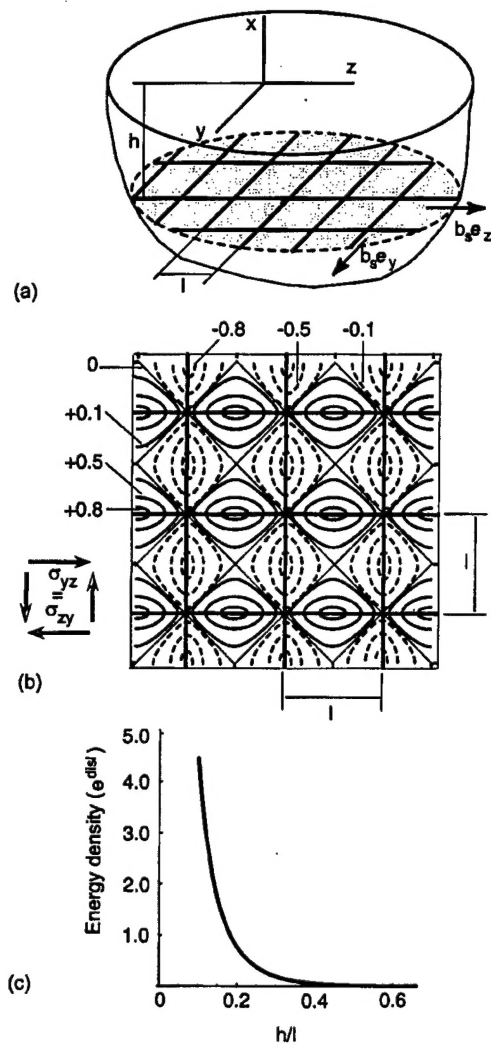[b]Electronic mail:speck@mrl.ucsb.edu

(a)

(b)

(c)

FIG. 1. Cross grid of screw dislocations in a subsurface layer. (a) Schematic representation of the dislocation arrangement in the subsurface layer. l is the spacing between dislocations and h is the distance of the cross grid from the free surface. (b) Contour plot of stress σ_{zy} at the surface due to screw dislocation cross grid; the stress is in units of $G\omega$. The solid horizontal and vertical lines show the position of the dislocations. The inclined thin lines correspond to zero stress contours. The positive and negative stress contours are shown as solid and dashed curved lines, respectively. (c) Dependence of the maximum change in energy density $e^{\mathrm{dis}l}$ (in units of $G\omega^2$) on the normalized distance h/l.

The elastic fields for the cross grid of screw dislocations have been found by summing the contributions of all individual dislocations. In this analysis, the stresses of an individual dislocation should satisfy boundary conditions at the free surface. For the case of a screw dislocation, the boundary conditions can be achieved with the aid of an image dislocation construction.[16] The only nonzero component of stresses at the surface ($x=0$) is given as

$$\sigma_{yz}=G\omega\sinh(2\pi\tilde{h})\left[\frac{1}{\cosh(2\pi\tilde{h})-\cos(2\pi\tilde{y})}\right.$$
$$\left.-\frac{1}{\cosh(2\pi\tilde{h})-\cos(2\pi\tilde{z})}\right], \quad (1)$$

where normalized values for y,z, and h ($\tilde{y}=y/l$, $\tilde{z}=z/l$ and $\tilde{h}=h/l$) are used, and G is the shear modulus. An example of the stress distribution for $\tilde{h}=0.25$ is shown in Fig. 1(b). It is clear from the figure that the stress field at the surface is periodic and nonuniform. For example, extreme values appear at the points directly above dislocation lines and halfway between dislocations of the orthogonal array. The stresses vanish directly above the dislocation intersections, as well as above the center of the square dislocation cells. As a result, the elastic energy density at the surface is also nonuniform. The distribution of elastic energy density $e^{\mathrm{dis}l}$ has fourfold symmetry and periodicity $l/\sqrt{2}$ which is aligned $45°$ with respect to the dislocation line directions. At the positions of maximum, the elastic energy density $e^{\mathrm{dis}l}$ has the following dependence on the distance of dislocations from the surface:

$$e^{\mathrm{dis}l}=G\omega^2\frac{2\sinh^2(2\pi\tilde{h})}{[\cosh^2(2\pi\tilde{h})-1]^2}. \quad (2)$$

The function $e^{\mathrm{dis}l}(\tilde{h})$ is shown in Fig. 1(c). The energy $e^{\mathrm{dis}l}$ gives a contribution to the dot nucleation energy that is controllable, thus inducing likely nucleation sites. It is useful to note that there is no interaction energy between the screw dislocations and the elastic field of the nucleating dots; the dot elastic field arises due to the dilatation misfit f with respect to surrounding material.

The interaction energy between quantum dots plays an important role in the vertical ordering of stacked dots.[5,7,13] To investigate this effect in detail, and also to compare it with the case of dislocations, we have calculated the elastic field of an array of buried dots. The precise shape of subsurface dots is still unknown and is a topic of controversy. However, it appears that the subsurface dots have a truncated pyramidal shape. Here, we model a single dot as an ellipsoidal inclusion with equal misfit f along its principal axes because there are known solutions in elasticity theory for this problem (which include the effects of the free surface). Furthermore, we believe that the general elastic features for the embedded dots can be reasonably represented by ellipsoidal inclusions since the size and size aspect ratio (or ratios) of the ellipsoidal inclusion can match those of a pyramidal inclusion. The geometry of the problem is given in the Fig. 2(a); inclusions with lengths c, d, and d along the x, y, and z axes, respectively (where we have used $d>c$) are located at distance h from the free surface of the nodes of square lattice with a periodicity l. The solution for the elasticity boundary value problem for a single ellipsoidal inclusion in such a geometry was given by Seo and Mura.[17] Using corrected expression from Ref. 17, the elastic strains of the inclusion array can be calculated for all material points, including the free surface. Figure 2(b) gives an example of the distribution of the trace of the stress tensor at the free surface $\sigma_{yy}+\sigma_{zz}$ (this is twice the biaxial hydrostatic stress) due to the subsurface dot array. For the case of a new quantum dot nucleating at the surface, the forming dots on the surface interact with buried dots; i.e., there exists preferential sites for dot nucleation at the surface due to the existing stress field. For an ellipsoidal inclusion, the maximum energy density release e^{dot} takes place directly above the buried dot, thus giving rise
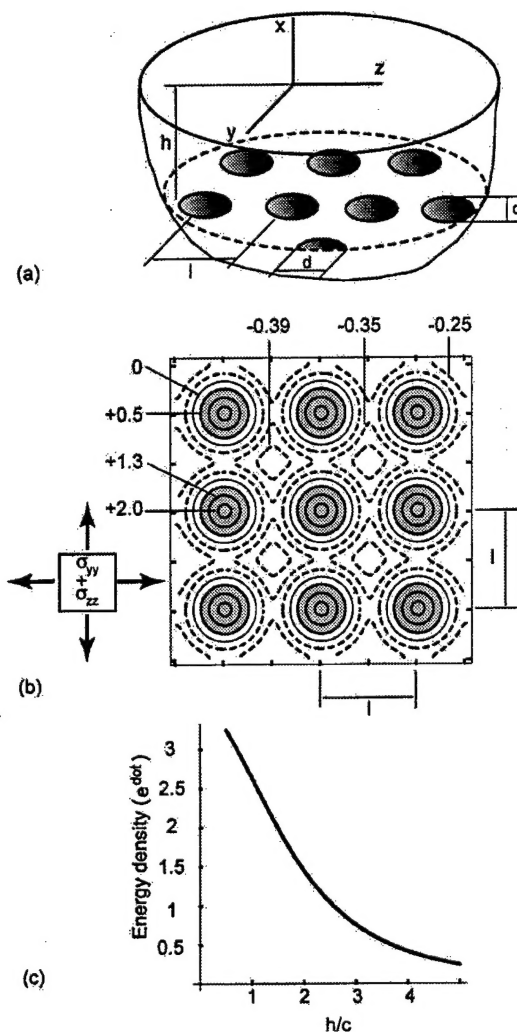
FIG. 2. An array of dots (dilatated inclusions) near a free surface. (a) An array of ellipsoidal inclusions with dimensions c, d, and d along the x, y, and z axes, respectively, at a distance h from the free surface; the misfit strain between the inclusion and matrix is f and the distance between inclusions is l. (b) Contour plot of twice the biaxial hydrostatic stress $\sigma_{yy}+\sigma_{zz}$ at the free surface due to buried inclusions; stress is in units of Gf. For the example shown here, $h=1.5c$, $d=3c$, and $l=6c$. The shaded circles show the position of the inclusions. Positive and negative stresses are shown by solid and dashed lines, respectively. (c) Dependence of the maximum change in the energy density e^{incl} (in units of Gf^2) on the normalized distance h/c. For this plot $d=5c$. In all calculations, Poisson's ratio v was taken as 0.3.

The value of ω depends on the misorientation induced by the cross grid of screw dislocations. For the case of $\omega = 0.0089$ rad ($=0.5°$), the dislocations have spacing $l = 115b_s$, or for a typical III–V material, e.g., GaAs, $l \sim 460$ Å. The misfit strain f can also vary in a broad range. For example, for $In_{0.5}Ga_{0.5}As$ dots in a GaAs matrix, $f = 0.033$. Therefore we assume that ω and f may have comparable magnitudes, but typically f may be a factor of ~ 2—5 larger than ω. Additionally, e^{dist} and e^{dot} have different dependencies on h. Due to the strong screening of the elastic fields of the cross grid of screw dislocations, e^{disl} has a rapid decay in h. It is known from experiments[5] that the effect of vertical ordering manifests itself for thicknesses $h/c \lesssim 3$. To reach the same magnitude of strain energy density at the surface, the dislocation cross grid should be placed at distance $h/l \sim 0.1$–0.2. For the values used above ($\omega = 0.5°$ and $b = 4$ Å), this would give fused layer thickness of ~ 50–100 Å, which is comparable to the layer thicknesses and twists experimentally demonstrated in twist wafer bonding for "compliant" substrates.[18] This estimate gives an upper limit for the thickness of the twisted layer, which is necessary to influence the quantum dot nucleation at the surface. Obviously, the use of a linear continuum elasticity description of dislocations is limited by the film thickness comparable with the dislocation core radius (where the theory of elasticity approach is not precise). However, this does not mean that the approach developed here cannot be applied to real fused layers, because the thickness of such layers for $h/l = 0.1$–0.2 still is enough to have at least tens of atom layers from the dislocation to the film surface, where therefore the effect of dislocation cores may be neglected.

[1] See, for example, A. Zunger, MRS Bull. **23**, 15 (1998) and related articles.
[2] D. Leonard, M. Krishnamurty, C. M. Reaves, S. P. DenBaars, and P. M. Petroff, Appl. Phys. Lett. **63**, 3203 (1993).
[3] D. Leonard, K. Pond, and P. Petroff, Phys. Rev. B **50**, 11687 (1994).
[4] Q. Xie, P. Chen, and A. Madhukar, Appl. Phys. Lett. **65**, 2051 (1994).
[5] S. Rouvimov, Z. Liliental-Weber, W. Swider, J. Washburn, E. R. Weber, A. Sasaki, A. Wakahara, Y. Furkawa, T. Abe, and S. Noda, J. Electron. Mater. **27**, 427 (1998).
[6] T. T. Ngo, P. M. Petroff, H. Sakaki, and J. L. Merz, Phys. Rev. B **53**, 9618 (1996).
[7] J. Tersoff, C. Teichert, and M. G. Lagally, Phys. Rev. Lett. **76**, 1675 (1996).
[8] D. Srolovitz, Acta Metall. **37**, 621 (1989).
[9] D. J. Eaglesham and M. Cerullo, Phys. Rev. Lett. **64**, 1943 (1990).
[10] H. Gao, J. Mech. Phys. Solids **39**, 443 (1991).
[11] L. B. Freund, Int. J. Solids Struct. **32**, 337 (1995).
[12] F. Jonsdottir and L. B. Freund, Mech. Mater. **20**, 337 (1995).
[13] V. A. Shchukin, D. Bimberg, V. G. Malyshkin, and N. N. Ledentsov, Phys. Rev. B , 12262 (1998).
[14] M. Grundmann, O. Stier, and D. Bimberg, Phys. Rev. B **52**, 11969 (1995).
[15] J. R. Downes, D. A. Faux, and E. P. O'Reilly, J. Appl. Phys. **81**, 6700 (1997).
[16] J. P. Hirth and J. Lothe, *Theory of Dislocations*, 2nd ed. (Wiley, New York, 1982).
[17] K. Seo and T. Mura, J. Appl. Mech. **46**, 568 (1979).
[18] F. E. Ejeckman, Y. H. Lo, S. Subramanian, H. Q. Hou, and B. E. Hammons, Appl. Phys. Lett. **70**, 1685 (1997).

to vertical ordering of the dots. The dependence of $e^{\text{dot}}(h/c)$ on the position of the buried dot is shown in the Fig. 2(c). Note in Figs. 2(b) and 2(c), we have used different d/c ratios to demonstrate the flexibility of our approach. In this analysis, we neglect the influence of neighboring buried dots, because for the set of typical experimental parameters, the contribution from neighboring dots is negligible.

To compare the influence of a dislocation cross grid and buried dot on the nucleation of new dots, we consider the characteristic dependencies of the energy densities on the parameters ω and f

$$e^{\text{disl}} \sim G\omega^2,$$

$$e^{\text{dot}} \sim Gf^2. \tag{3}$$

Controlled ordering and positioning of InAs self-assembled quantum dots*

H. Lee, J. A. Johnson, J. S. Speck, and P. M. Petroff[a]

Materials Department, University of California, Santa Barbara, California 93106

An experimental approach has been developed to control the formation of InAs self-assembled islands. A lithographically defined mesa lattice on the surface was used to control the growth kinetics and island nucleation. Two distinct island formation regimes were observed from InAs islands grown on patterned GaAs (100) substrates. In the case of direct growth on patterned substrates, a type I islanding was observed, in which all the islands formed between mesas. Incorporating a stressor layer into the regrowth on the patterned substrate yielded a type island nucleation, where all the islands nucleated on top of the mesas. The possible mechanisms involved in the long range ordering and positioning of islands are discussed. © *2000 American Vacuum Society.* [S0734-211X(00)06604-X]

I. INTRODUCTION

Self-assembled quantum dots (QDs) have been intensely studied in the last several years due to their appealing electronic and optical properties.[1-3] Unique physical properties have been observed in QD structures[4,5] and device applications using QDs, such as lasers, detectors, and memories have been explored.[6-8] The self-assembled growth of QDs relies on the strain induced island formation via the Stranski–Krastanow growth mode,[3] in which island formation is the first step to minimize strain energy in coherent heteroepitaxial layers.[9] Many lattice-mismatched systems, such as InAs/GaAs, Ge/Si, and InAs/InP, have been investigated with the aim of understanding and controlling island formation.[10-21] In particular, the interplay between island nucleation and surface patterning has been studied extensively. This has been done for both larger features defined by conventional lithography[13-19] and for nano-scale inclusions patterned using electron beam techniques.[20,21] Subsurface strain fields have also been shown to play a controlling role in island nucleation, as seen in vertically stacked QDs.[2,10,11] The use of strain coupling has been extended to the highly anisotropic PbSe/PbEuTe system to produce excellent three-dimensional (3D) quantum dot lattices.[22] Despite all these efforts, the ability to control the positioning of III–V islands remains limited and this poses a great hurdle to the incorporation of QDs into devices.

We extend these ideas by using a technique, which combines lithography with *in situ* lateral strain engineering to restrict the island nucleation to mesoscopic areas of the wafer surface. In our experiments, submicron mesa arrays were fabricated using holographic lithography and wet chemical etching. Strain engineering was achieved by incorporating a coherently strain $In_{0.2}Ga_{0.8}As$ layer, which we call stressor, into the regrown structure. Due to the patterned features, the strain of the $In_{0.2}Ga_{0.8}As$

was modulated and energetically favorable nucleation sites were created on top of the mesas. Excellent long range island ordering is obtained. In this article, details of our technique will be discussed and both results of islands formed without stressor (type I nucleation) and with stressor (type II nucleation) will be presented and compared. Strong photoluminescence was also observed from these InAs QDs grown on patterned substrates.

II. EXPERIMENT AND DISCUSSION

Ordering of InAs self-assembled QDs on mesa lattices was promoted by deposition of InAs under favorable growth kinetics and thermodynamic conditions. Two distinct sets of regrowth structures, which corresponded to types I and II islanding, were studied. They are illustrated in Fig. 1. As will be shown, engineering of the regrowth structure on the mesa lattices allows a control of the island nucleation site positioning.

A. Defining the mesa lattices

Holography was used to pattern the GaAs (001) substrates, since it provided a simple and efficient method to create nanoscale mesa lattices over large areas. In this process, a GaAs substrate was first coated with photoresist (Shipley 1400-4) and then exposed in a holographic apparatus twice, with the sample rotated 90° after the first exposure. The patterns were transferred onto the GaAs substrates by wet chemical etching using $H_3PO_4:H_2O_2:H_2O=3:1:75$. The resulting pattern was a checkerboard array of square mesas. The unit cell of the lattice was 250 nm×250 nm. The mesas resembled truncated pyramids 25 nm high with a base width of 170 nm and top dimension <20 nm. Holography is very flexible, as it is easy to adjust the mesa dimensions, spacing, and orientation. In this study, we explored two different mesa lattice orientations. One lattice had its unit cell aligned along ⟨110⟩ (type A) and the other was rotated to aligned along ⟨100⟩ (type B). In these two different orientations, mesas had similar shape but were bound by different facets. After overgrowth, they showed distinct features, as described below.
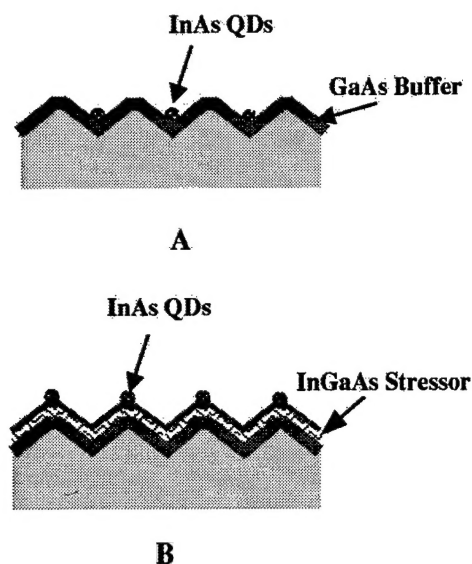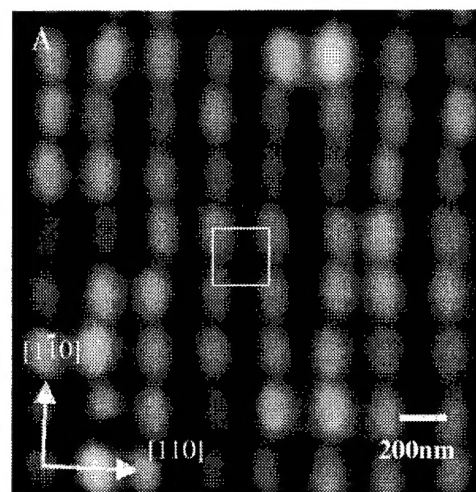
FIG. 1. Sample structures for two types of regrowth. (a) Schematic of the type I islanding. (b) Schematic of type II islanding.

(a)

(b)

FIG. 2. AFM images of regrowth after 40 nm GaAs. (a) on type "A" mesa lattice and (b) on type "B" mesa lattice. The unit cell of each lattice is also indicated.
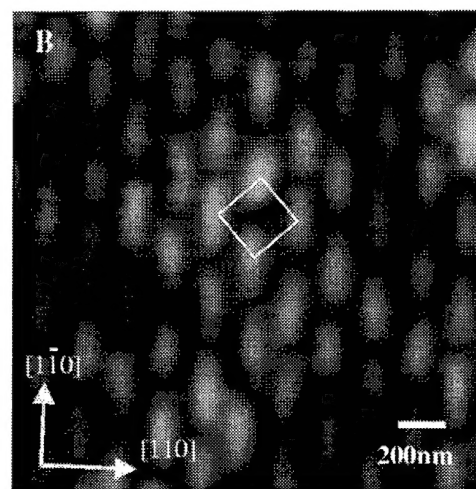
B. Regrowth of the GaAs buffer layer on patterned GaAs surfaces

Before introduction into the molecular beam epitaxy (MBE) system, the patterned GaAs substrates were thoroughly cleaned in solvents and a fresh oxide layer was formed after a 10% HCl etch. The MBE regrowth started with a thermal desorption of the oxide layer under As_2 flux (5×10^{-6} Torr) at 630 °C. It was followed by the growth of a GaAs buffer layer at 600 °C. In situ reflection high energy electron diffraction (RHEED) was used to monitor the surface. Since a thin buffer layer was needed to preserve the surface patterned features, multiple growth interruptions (10 s every 5 nm) were used during the deposition to accelerate surface recovery from damages associated with processing and oxide desorption.

Figure 2 shows atomic force microscopy (AFM) images of the mesa lattices surfaces after 40 nm of GaAs was deposited on the two types of mesa patterns. In Figs. 2(a) and 2(b), the images show the evolution of lattices, which prior to regrowth had unit cell vectors parallel to $\langle 110 \rangle$ and $\langle 100 \rangle$ directions, respectively. Mesas in both lattices elongated in the $[1\bar{1}0]$ direction giving new mesa base dimensions on the order of 200 nm $\times$ 300 nm. The mesas height was reduced to 5 nm and the top was flattened to 50 nm $\times$ 200 nm. The observed anisotropic growth is quite common in MBE of III–V compounds. It is caused by the different diffusion rates in the two $\langle 110 \rangle$ directions and enhanced by the multiple growth interruptions during the GaAs buffer layer deposition. Associated with this elongation, the individual mesa in the type A lattice (along $\langle 110 \rangle$) has developed new facets. In this case, the facets on each mesa evolved from $\{10m\}$ to $\{11n\}$.

C. Growth of InAs island on patterned substrates

After the GaAs buffer layer was grown at 600 °C, the substrate temperature was lowered to 530 °C to deposit InAs islands. We used RHEED to monitor the island formation. The characteristic streaky to spotty RHEED pattern transition was observed after 1.7 ML of InAs were deposited, thus indicating the onset of 3D islands formation.[13,23] AFM images of InAs QDs on both mesa orientations with 40 nm GaAs buffer layer are shown in Fig. 3. These images show a type I islanding, in which the islands are formed between mesas.

As Fig. 3(a) shows, distinct one-dimensional (1D) ordered island arrays were obtained on type A mesa lattices. These preferred island nucleation sites are characteristic of type A mesa lattices only and may be a direct consequence of the mesa facet evolution during the GaAs buffer layer growth. Figure 3(b) shows the results of a growth sequence similar to
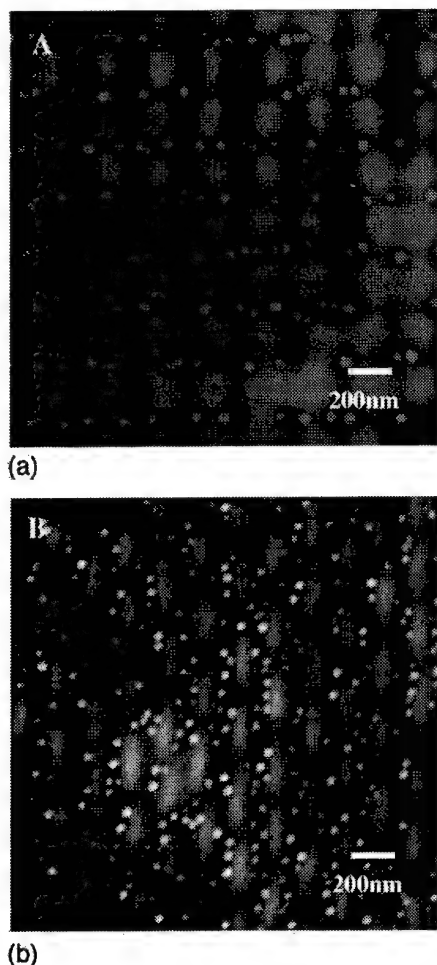
(a)

(b)

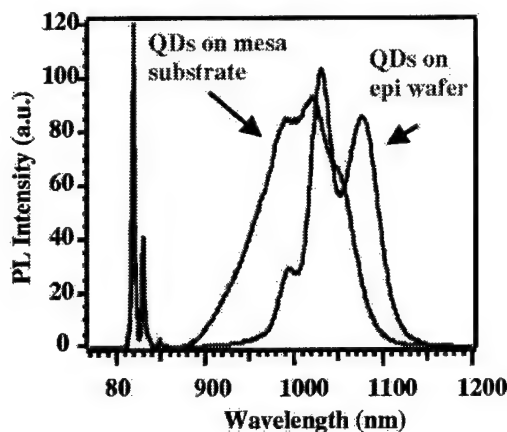FIG. 3. AFM images of InAs QDs on (a) type "A" mesas and (b) on type "B" mesas.

FIG. 4. Photoluminescence spectra from InAs QDs grown on patterned and unpatterned substrates at 3 K.

excite the QDs with a power density of 10 kW/cm^2. For comparison, we also show a PL spectrum of an unpatterned sample grown at the same time as the patterned sample. The PL intensity from the QDs on patterned substrates is comparable to that of an unprocessed sample. Excited states are also observed at this pumping density. The energy of the

that used in Fig. 3(a) but for a "B" mesa lattice. In both "A" and B type mesa lattices, all the islands were located in the valleys between the mesas. Similar results were obtained for InAs deposited on 60 nm GaAs buffer layers. The island diameter formed on patterned substrates ranged from 27 to 40 nm and their sizes appeared to be larger than on planar substrates (22–30 nm).

A possible explanation for the type I islanding is as follows. To minimize surface energy, concave regions will tend to fill and planarize upon overgrowth.[24] In the initial stages of QD deposition on the mesa arrays, the growth of the InAs wetting layer may be enhanced in the valleys due to the negative mean curvature. The wetting layer reaches the critical thickness rapidly inside the valleys, triggering the two-dimensional (2D) to 3D growth transition. Hence, the islands grow preferentially between the mesas. This explanation also accounts for the larger sized islands found between the mesas, compared to those on the planar surface.

Efficient photoluminescence (PL) was observed from type I islands after they were capped with 40 nm GaAs. The PL spectra shown in Fig. 4 were collected at 3 K with a cooled InGaAs photomultipler tube. An Ar-ion laser was used to
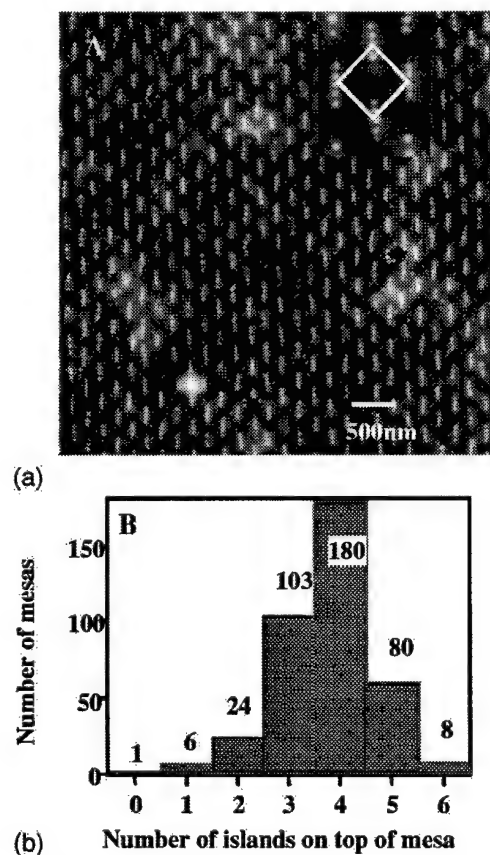

(a)

(b)

FIG. 5. (a) AFM images of InAs QDs grown on a patterned substrate with a 20 nm In$_{0.2}$Ga$_{0.8}$As stressor layer. (b) Histogram of the number of islands found on top of the mesas.

ground state PL line (1.18 eV) for the InAs QDs grown on mesa lattices is blue shifted 34 meV with respect to the unpatterned sample. This also indicates that islands formed on patterned surfaces differ in size and composition. The strong PL signal observed from the InAs QDs grown on patterned substrates attests of the good quality of the InAs QDs and it indicates our regrowth surface has recovered from processing damages.

D. Growth of InAs QDs on mesa tops

A second nucleation regime can be achieved by introducing strain into the regrowth. By adding a strained $In_{0.2}Ga_{0.8}As$ layer after the GaAs buffer, the preferential nucleation of the QDs on mesa tops, type II islanding, was achieved. The sample structure, illustrated in Fig. 1(b), was a 60 nm GaAs buffer layer grown at 600 °C, followed by a 20 nm $In_{0.2}Ga_{0.8}As$ stressor layer, and 10 nm GaAs grown at 510 °C. The InAs islands were then deposited at 530 °C. An AFM image of InAs islands grown on a type B patterned substrate with stressor layer is shown in Fig. 5(a). The majority (over 90%) of InAs QDs were formed on top of mesas. Excellent island position control and long range 2D ordering were achieved with the use of a stressor layer. For this mesa size, there were on average close to four islands on top of each mesa, as indicated by the histogram shown in Fig. 5(b). Type A mesa arrays, with the same regrowth conditions, also exhibited long range QD ordering with the islands nucleating on top of the mesas.

The effect of the stressor layer on the mesa island positioning is critical. Islands on top of the mesas are analogous to the observed vertical stacking of quantum dots. Due to the patterning, the stressor layer can partially relax at the mesas peak, thus locally straining the thin GaAs barrier above the $In_{0.2}Ga_{0.8}As$. When the quantum dots are deposited, InAs preferentially accumulates where the strain energy is minimized on the growth surface,[25] i.e., at the mesa tops. The thickness and composition of the stressor layer is crucial for partial strain relaxation to occur effectively at the mesas. Indeed, for an $In_{0.2}Ga_{0.8}As$ stressor below 5 nm, all the islands are found in the valleys between mesas. The driving force to nucleate islands on top of the mesas must exceed the tendency for In to accumulate in the valleys as in type I nucleation. Detailed modeling of pattern induced strain modulation in type II structures will be discussed in a forthcoming publication.

III. SUMMARY

The present work demonstrates that control of the nucleation site positioning of InAs self-assembled QDs can be achieved by MBE deposition on a GaAs surface with a mesa lattice. Long range ordering is imposed by the presence of the mesas and/or by the introduction of a stressor layer. These techniques produce optically active QDs and provide a promising route for many device applications.

[1]Y. Arakawa and H. Sakaki, Appl. Phys. Lett. **40**, 939 (1982).
[2]L. Goldstein, F. Glas, J. Y. Marzin, M. N. Charasse, and G. Le Roux, Appl. Phys. Lett. **47**, 1099 (1985).
[3]D. Leonard, M. Krishnamurthy, C. M. Reaves, S. P. DenBaars, and P. M. Petroff, Appl. Phys. Lett. **63**, 3203 (1993).
[4]H. Drexler, D. Leonard, W. Hansen, J. P. Katthaus, and P. M. Petroff, Phys. Rev. Lett. **73**, 2252 (1994).
[5]J. -Y. Marzin, J. -M. Gerard, A. Izrel, D. Barrier, and G. Bastard, Phys. Rev. Lett. **73**, 716 (1994).
[6]N. Kirstaedter, N. N. Ledentsov, M. Grundmann, D. Bimberg, V. M. Ustinov, S. S. Ruvimov, M. V. Maximov, P. S. Kopev, Z. I. Alferov, U. Richter, P. Werner, U. Gosele, and J. Heydenreich, Electron. Lett. **30**, 1416 (1994).
[7]D. Pan, E. Towe, and S. Kennerly, Appl. Phys. Lett. **73**, 1937 (1998).
[8]T. Lundstrom, W. Schoenfeld, H. Lee, and P. M. Petroff, Science **286**, 2312 (1999).
[9]J. Tersoff and F. K. LeGoues, Phys. Rev. Lett. **72**, 3570 (1994).
[10]Q. Xie, A. Madhukar, P. Chen, and N. P. Kobayashi, Phys. Rev. Lett. **75**, 2542 (1995).
[11]G. S. Solomon, J. A. Trezza, A. F. Marshall, and J. S. Harris, Phys. Rev. Lett. **75**, 952 (1996).
[12]H. Lee, R. Lowe-Webb, W. Yang, and P. C. Sercel, Appl. Phys. Lett. **71**, 2325 (1997).
[13]D. S. L. Mui, D. Leonard, L. A. Coldren, and P. M. Petroff, Appl. Phys. Lett. **66**, 1620 (1995).
[14]A. Konkar, R. Heitz, T. R. Ramachandran, P. Chen, and A. Madhukar, J. Vac. Sci. Technol. B **16**, 1334 (1998).
[15]W. Seifert, N. Carlsson, A. Petersson, L. -E. Wernersson, and L. Samuelson, Appl. Phys. Lett. **68**, 1684 (1996).
[16]R. Tsui, R. Zhang, K. Shiralagi, and H. Goronkin, Appl. Phys. Lett. **71**, 3254 (1997).
[17]T. I. Kamins and R. S. Williams, Appl. Phys. Lett. **71**, 1201 (1997).
[18]S. Jeppesen, M. S. Miller, D. Hessman, B. Kowalski, I. Maximov, and L. Samuelson, Appl. Phys. Lett. **68**, 2228 (1996).
[19]G. Jin, J. L. Liu, S. G. Thomas, Y. H. Luo, K. L. Wang, and B. -Y. Nguyen, Appl. Phys. Lett. **75**, 2752 (1999).
[20]T. Ishikawa, S. Kohmoto, and K. Asakawa, Appl. Phys. Lett. **73**, 1712 (1998).
[21]S. Kohmoto, H. Nakamura, T. Ishikawa, and K. Asakawa, Appl. Phys. Lett. **75**, 3488 (1999).
[22]G. Springholz, V. Holy, M. Pinczolits, and G. Bauer, Science **282**, 734 (1999).
[23]Y. Nabetani, T. Ishikawa, S. Noda, and A. Sasaki, J. Appl. Phys. **76**, 3347 (1994).
[24]M. Ozdemir and A. Zangwill, J. Vac. Sci. Technol. A **10**, 684 (1992).
[25]J. Tersoff, C. Teichert, and M. G. Lagally, Phys. Rev. Lett. **76**, 1675 (1996).

Elastic fields of quantum dots in subsurface layers

A. E. Romanov
A. F. Ioffe Physico-Technical Institute, Russian Academy of Sciences, 194021 St. Petersburg, Russia

G. E. Beltz and W. T. Fischer
Department of Mechanical and Environmental Engineering, College of Engineering, University of California, Santa Barbara, California 93106

P. M. Petroff and J. S. Speck[a]
Materials Department, College of Engineering, University of California, Santa Barbara, California 93106

In this work, models based on conventional small-strain elasticity theory are developed to evaluate the stress fields in the vicinity of a quantum dot or an ordered array of quantum dots. The models are based on three different approaches for solving the elastic boundary value problem of a misfitting inclusion embedded in a semi-infinite space. The first method treats the quantum dot as a point source of dilatation. In the second approach we approximate the dot as a misfitting oblate spheroid, for which exact analytic solutions are available. Finally, the finite element method is used to study complex, but realistic, quantum dot configurations such as cuboids and truncated pyramids. We evaluate these three levels of approximation by comparing the hydrostatic stress component near a single dot and an ordered array of dots in the presence of a free surface, and find very good agreement except in the immediate vicinity of an individual quantum dot. © 2001 American Institute of Physics. [DOI: 10.1063/1.1352681]

I. INTRODUCTION

Self-assembled quantum dots (SAQDs) have attracted substantial recent attention because they offer the potential for three-dimensional confinement of carriers and excitons and have "atom-like" electronic states.[1,2] SAQD formation is commonly observed in large mismatch epitaxy of chemically similar materials.[1,3] For example, the Stranski–Krastanow (SK) growth of InAs (or $In_xGa_{1-x}As$) on GaAs first involves the growth of a ~1 to 2 monolayer thick "wetting layer" followed by coherent island formation.[1,3] The SAQDs may be buried by the growth of the same materials as the underlying substrate. Subsequent growth of the strained composition on the buried dot template has been shown to lead to vertical stacking of dots provided that the thickness of the intervening layer ("spacer layer") is in the order or thinner than the lateral dimensions of the dot.[4]

It is now clear that dot ordering is driven by the elastic field of subsurface stressors. Usually, these subsurface stressors are buried dots themselves (which give rise to vertical ordering).[4–9] In group IV and III–V SAQD growth, the first dot layer does not demonstrate lateral order and subsequent layers show only vertical ordering (however, other subsurface stressors such as regular dislocation arrays[10] or buried strained layers grown on patterned substrates[11] can initiate lateral ordering). Buried subsurface stressors lead to a modulation in the stress field and associated strain field on the growth surface which affects both adatom diffusion[12] and SK island nucleation rates.[13]

The strain fields caused by SAQDs strongly affect the electronic properties in the vicinity of the dots.[14–19] Two

strain effects are predominant in the electronic properties of III–V semiconductors: changes in the conduction and valence band levels (deformation potentials) and local electric fields due to piezoelectric effects. The conduction band is only affected by the hydrostatic strain, often referred to as the dilatation or trace of the strain tensor. The valence levels can change both with hydrostatic and shear strain. For zinc blende structures, deviatoric strains (those strains which differ from pure hydrostatic strains) give rise to piezoelectrically induced electric fields.[16] In the general case for zinc blende SAQDs, strain causes negligible change in the confined energy levels within the dots, however, the conduction and valence levels can be changed in the surrounding matrix. Further, strain can cause local piezoinduced electric fields within the dots and in the surrounding matrix.[18] Additionally, strain can strongly modify the phonon frequencies within the dots in the surrounding material.[17]

Both for understanding ordering and the effects on electronic properties, it is important to determine the full elastic fields in the dots and surrounding matrix. The elastic fields depend on the lattice mismatch between the dot and matrix material, the elastic properties of both the dot and the matrix, the dot shape, and the position of dot with respect to the free surface. A complete solution of the elasticity problem in the most general case is not possible in closed analytical form. Independent of quantum dots, the general inclusion problem was extensively developed in the pioneering work of Eshelby[20,21] and we address this approach in the next section. In the SAQD field, three main methods have been applied to determine the elastic strains and stresses, namely: (i) theory of inclusions based on the analytical solution of elasticity equations ("Eshelby-like" or related approaches),[8,14,16,22–24] (ii) finite element methods (FEM),[25–28] and (iii) atomistic

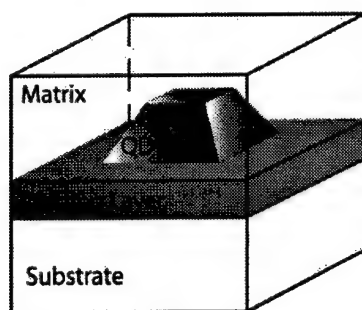[a] Electronic mail: speck@mrl.ucsb.edu

FIG. 1. General schematic of a buried quantum dot (QD). A wetting layer (WL) is shown, which may precede the formation of an island during the deposition of a dissimilar material onto a substrate. The island (quantum dot) is subsequently covered by additional matrix (substrate) material.

modeling.[29–31] The theory of inclusions provides integral expressions for elastic fields which can be integrated in closed form only for the simplest inclusion shapes, such as cylinders or spheres. Even with the simplification of isotropic elasticity, the known application to quantum dots so far have neglected the effects of the free surface. FEM is very effective for particular cases but does not provide general solutions and is furthermore affected by the choice of boundary conditions for the modeling domain. Atomistic models require accurate interatomic potentials and are further restricted to small systems of atoms in comparison with dot sizes and the surrounding matrix.

In this article we apply two analytic approaches for SAQD mechanics which include the effect of the free surface and the dot shape and compare these results with FEM calculations. We concentrate on the far field solutions in the analytic approaches, as our main interests are related to dot ordering. However, we believe the analytic solutions are useful for determining the strain effects on the electronic structure of the matrix.

II. MODELING OF QUANTUM DOTS

From a continuum mechanics viewpoint, a quantum dot can be thought of as an inclusion of some prescribed shape embedded in a dissimilar matrix. Due to compositional differences which give rise to a lattice parameter mismatch or possibly a thermal expansion mismatch, the inclusion and surrounding matrix will be under a residual state of stress. Moreover, the inclusion may possesses different elastic moduli from the matrix material. Assuming a linear elastic response, the resulting stress fields for such problems are very cumbersome and have only been worked out analytically for limited geometries, including cuboids[32,33] and ellipsoids[34,35] in infinite and semi-infinite domains. For the case of an ellipsoid in an infinite matrix, the solutions for this class of problems were originally developed by Eshelby in the 1950s.[20,21]

Figure 1 shows a schematic based on experimental observations, in which a wetting layer initially forms when a material of new composition is deposited onto a substrate. After the wetting layer achieves several monolayers of thickness, an instability in growth leads to isolated island formation (future quantum dots).[1,3,4] Currently, there are also indi-

cations that the wetting (transitional) layer may be much thicker (comparable with the dot height) and may possess different chemical composition than nucleating quantum dots. We do not address this issue in this article. Rather, we only consider the elastic field from the dot itself and do not consider the wetting. Although there is another controversy over the actual shape of quantum dots, it is clear from transmission electron microscopy (TEM) studies that they initially form as four-sided pyramids. Truncation of capped pyramids may be an illusion induced by strain fields observed by TEM. This possibility is supported by researchers reporting detailed contrast evidence in favor of sharp-capped pyramids.[4] This controversy has implications for the present finite-element study. However, upper levels of pyramidal dots are relatively unstrained, and therefore would add little mechanical energy. For this reason, it is believed that the question of pyramid truncation will not have a pronounced effect on the conclusions to be obtained by modeling.

In this article we propose a number of simplified models to describe the elastic field surrounding a quantum dot. The simplest approach is to ignore the geometry of the dot altogether, and to regard it as a point source of dilatation of prescribed strength fV, where f represents the mismatch and V represents the volume of an "equivalent" dot, that is, the real dot that is being simulated by the point source. The parameter f represents the strain state developed in the quantum dot, relative to an equivalent volume of matrix material, if it were not constrained by the matrix; for example, if a dot with lattice parameter a_d is deposited onto a substrate surface with lattice parameter a_s, the misfit strain f is taken as $(a_s - a_d)/a_d$. When the island is subsequently surrounded by matrix material, the constraint is uniform in three directions; hence the misfit strain components become $f\delta_{ij}$. Similarly, a thermal expansion mismatch gives rise to such a dilatational self-strain (also known in the literature as the stress-free strain or the "eigenstrain"), so all sources of misfit may be incorporated into the single parameter f. Of course, such an approach is expected to yield expressions that break down in the general vicinity of the dot.

A powerful method for the solution of a broad spectrum of problems in elasticity derives from a consideration of point forces applied at some point in the elastic body.[36,37] If the response of a body to a point force (i.e., the Green's function) is known, the deformation caused by any distribution of forces can be obtained by superposition. For example, the displacement field caused by a single point force applied anywhere in an infinite elastic solid may be determined quite straightforwardly from the field equations of elasticity.[37] If the body is finite, as in the case of a semi-infinite space, a traction-free boundary condition must be satisfied, thereby giving a corrective term to the displacement field for an infinite solid.

In the case of a point source of expansion, three mutually perpendicular pairs of forces (each pair consists of a dipole of opposing forces of magnitude P, separated by a distance d along their mutual line of action) may be used (see Fig. 2). If one considers a cube of volume $V = d^3$, the average stress in the cube is P/d^2, which in turn can be related to the strains arising from the misfit f via Hooke's law. Apply-
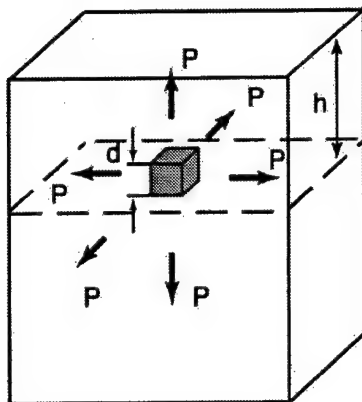
FIG. 2. Point source of dilatation at distance h from a free surface, represented as a cube with infinitely small dimension d. Three force dipoles P are applied to the faces of this cube.
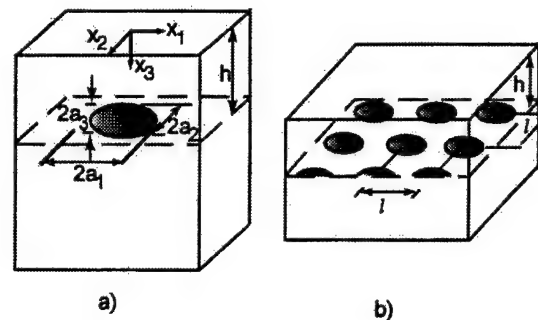

FIG. 3. Ellipsoidal inclusions used to model quantum dots. (a) An isolated ellipsoidal inclusion at distance h from the surface, with semiaxes a_1, a_2, and a_3 in the corresponding coordinate directions. (b) A rectangular array of the same ellipsoidal inclusions, with periodicity ℓ in the lateral coordinate directions.

ing such an argument to an isotropic medium, one may arrive at the relation $Pd = [2(1+\nu)\mu/(1-2\nu)]fV$, where μ is the material shear modulus and ν is Poisson's ratio. By taking the limit as $d \to 0$, maintaining Pd constant, the complete elastic field for a point of expansion of a given strength may be identified. Mindlin[38] and Mura[34,35] have provided the appropriate expressions for such point sources, not only for a generally anisotropic medium, but also for a point source located in a semi-infinite, isotropic medium. The primary advantage with this method is that the expressions are compact, especially for the case of an isotropic medium, as illustrated in Sec. III A.

The next level of complexity would be to idealize the quantum dot as an inclusion of some simplified shape, such as spherical, ellipsoidal, or cuboidal. Mura[34,35] has developed expressions for an ellipsoidal inclusion in a half-space in an extension of the point-source analysis described above by integrating the appropriate Green's function over the volume of the inclusion. Chiu[32,33] has provided similar results, but for a cuboidal inclusion embedded in a semi-infinite medium. Despite these relatively simple shapes, closed form solutions are only possible for the ellipsoid when at least two of the semiaxes are identical, as demonstrated below. In the example to be discussed in Sec. III B, an oblate spheroid (an ellipsoid with semiaxes $a_1 = a_2 > a_3$), a depth h from the surface, will be considered, either alone or as an ordered array of spacing l (see Fig. 3). Although the stress expressions are more cumbersome than for the point sources of dilatation (as given below in Sec. III B), the advantage is that a more realistic idealization of the quantum dot geometry is achieved, and in such a way that the effect of the aspect ratio of the dot may be efficiently evaluated.

For the case of quantum dots with extreme aspect ratios, for example, a relatively flat square or "penny-shaped" quantum dot, the stress field may be approximated as that due to an appropriately shaped prismatic dislocation loop, the stress fields for which are well-known. As the quantum dot deviates from an extreme aspect ratio, this method still works, because the shape may be represented by an array of prismatic dislocation loops. Li[39] and Gutkin and coworkers[40,41] have exploited this equivalence for determin-

ing the stress fields around various inclusion shapes, albeit in a different context from quantum dot behavior. For the sake of brevity, we do not outline this method in this article.

The final level of complexity undertaken in this article is to evaluate the complete stress field in the vicinity of a cuboidal or trapezoidal inclusion via the finite element method (FEM). In other words, we model the geometries similar to that of Fig. 1, excluding the wetting layer. The FEM models can easily be expanded to include the wetting layer (see, for example, Ref. 28); however, we do not undertake that here since the primary goal is to make comparisons with the quantum dot models based on point sources and ellipsoidal inclusions mentioned earlier. For a typical trapezoidal inclusion within a matrix unit cell, elastic solutions may be approximated using a finite element mesh comprising one quadrant of an arbitrarily deep matrix unit cell, with appropriate boundary conditions imposing symmetry at the lateral faces (see Sec. III C). The primary advantage with this method is that more details concerning the stress field may be revealed, especially near the sharp corners of the inclusion. The FEM technique can readily include elastic anisotropy combined with different elastic constants for the matrix and the dot. The disadvantage is that a mesh must be created for each dot geometry, and the size of the matrix mesh must be made arbitrarily large in order to compare these results with those of the point source or the inclusion.

To simulate this residual strain in the model presented here, perfect bonding is assumed, and strains are imparted by a "phantom" thermal expansion mismatch between the inclusion and the matrix. Of course, in the system simulated, thermal expansion mismatch may or may not be a significant effect. However, since the effect of introducing such a differential expansion is to change the zero-stress lattice size for both materials, there is no analytical difference between differential strains induced by lattice mismatch, and those induced by thermal expansion mismatch.

III. ELASTIC SOLUTIONS FOR SUBSURFACE QUANTUM DOT STRESSORS

A. Point source of dilatation

For the case of a single point source of expansion located a distance h from the surface, the displacement field is

given by Mura.[34,35] We have differentiated that expression to obtain strain through the relation $\varepsilon_{ij} = \frac{1}{2}(u_{i,j} + u_{j,i})$ and subsequently used Hooke's law, $\sigma_{ij} = 2\mu(\varepsilon_{ij} + [\nu/(1-\nu)]\delta_{ij}\varepsilon_{kk})$ to obtain the result

$$\sigma_{ij} = \frac{\mu f V(1+\nu)}{2\pi(1-\nu)}\left[-\left(\frac{1}{R_1}\right)_{,ij} - x_3\left(\frac{2}{R_2}\right)_{,3ij}\right.$$
$$+ (3-4\nu)(\delta_{3i}+\delta_{3j}-1)\left(\frac{1}{R_2}\right)_{,ij} - \delta_{3j}\left(\frac{1}{R_2}\right)_{,3i}$$
$$\left.- \delta_{3i}\left(\frac{1}{R_2}\right)_{,3j} + \nu\delta_{ij}\left(\frac{4}{R_2}\right)_{,33}\right], \tag{1}$$

where, as before, μ is the shear modulus, ν is the Poisson's ratio, f is the mismatch, V is the dot volume, and δ_{ij} is the Kronecker delta. The quantities R_1 and R_2 are given by $\sqrt{x_1^2+x_2^2+(x_3-h)^2}$ and $\sqrt{x_1^2+x_2^2+(x_3+h)^2}$, respectively. The notation $(\,)_{,i}$ indicates $\partial/\partial x_i()$ while repeated indices are summed from 1 to 3. The use of a finite volume in these formulas is an approximation, as discussed in the previous section, since the expressions really derive from differential equations and are exact for the case of a vanishingly small inclusion. These expressions are expected to only yield realistic results when considering target distances compared with the characteristic length of the quantum dot, for example, the stresses at the surface for cases where the quantum dots are buried sufficiently beneath the surface.

In order to graphically illustrate the stress distribution near a quantum dot and to facilitate comparisons with other, more precise representations of the stress field, we use the trace of the stress tensor σ_{kk} rather than individual components. This component is the key quantity for calculating the interaction energy between a quantum dot and an adatom on the surface, and thus the driving force for adatom diffusion at the surface. The trace is related to the pressure through the relation $p = -\frac{1}{3}\sigma_{kk}$ and is given by

$$\sigma_{kk} = \frac{2\mu f V(1+\nu)^2}{\pi(1-\nu)}\left(\frac{1}{R_2}\right)_{,33}$$
$$= \frac{2\mu f V(1+\nu)^2}{\pi(1-\nu)}\frac{[2(x_3+h)^2 - x_1^2 - x_2^2]}{[x_1^2+x_2^2+(x_3+h)^2]^{5/2}}. \tag{2}$$

The local dilatation, ε_{kk}, is given by $-p[3(1-2\nu)/2\mu(1+\nu)]$, where the quotient of elastic constants is the inverse of what is referred to as the bulk modulus. The dilatation is of interest due to its effect on the electronic band structure in and near the quantum dot[16] and on dot nucleation and growth due to the surface diffusion.[12] We note that in Eqs. (1) and (2), all terms containing R_1 comprise the solution for the case when the point source is embedded in an infinite medium, and the terms with R_2 represent the correction due to the presence of the free surface. Hence $\sigma_{kk} = 0$ for an infinite solid but not for the semi-infinite solid. The effect of the free surface on the dilatation field of various inclusions was studied in greater detail by Michel *et al.*[42,43]

For the case of an ordered array of quantum dots (see Fig. 3), the stress field can be obtained by summing Eq. (1)

or Eq. (2) over all dots. For a square array of dots of spacing ℓ, the trace of the stress tensor at all locations is given by

$$\sigma_{kk} = \frac{2\mu f V(1+\nu)^2}{\pi(1-\nu)}$$
$$\times \sum_{i=-\infty}^{\infty}\sum_{j=-\infty}^{\infty}\frac{[2(x_3+h)^2 - (x_1-i\ell)^2 - (x_2-j\ell)^2]}{[(x_1-i\ell)^2+(x_2-j\ell)^2+(x_3+h)^2]^{5/2}}, \tag{3}$$

where h represents the depth of the planar array of dots. The double sum represented in Eq. (3), to our knowledge, has no analytic representation; however, it can be numerically evaluated by replacing ∞ with some suitably large integer.

B. Ellipsoidal dilatated inclusion

As shown by Mura,[34,35] the stress field for an ellipsoidal inclusion in a half space can be obtained by integrating the displacement field that gave rise to Eq. (1) over the domain

$$\frac{x_1'^2}{a_1^2} + \frac{x_2'^2}{a_2^2} + \frac{(x_3'-h)^2}{a_3^2} \leq 1, \tag{4}$$

where a_1, a_2, and a_3 denote the semiaxes of the ellipsoid along the respective coordinate directions, and h denotes the depth of the center of the ellipsoid from the surface. For points exterior to the inclusion, the stress components take the form

$$\sigma_{ij} = \frac{\mu f V(1+\nu)}{2\pi(1-\nu)}[-\psi_{,ij} - 2x_3\phi_{,3ij} + (3-4\nu)$$
$$\times(\delta_{3i}+\delta_{3j}-1)\phi_{,ij} - (\delta_{3i}+\delta_{3j})\phi_{,ij} + 4\nu\delta_{ij}\phi_{,33}], \tag{5}$$

where

$$\psi = \frac{3}{4}\int_\lambda^\infty \frac{1 - \left(\frac{y_1^2}{a_1^2+s} + \frac{y_2^2}{a_2^2+s} + \frac{y_3^2}{a_3^2+s}\right)}{\sqrt{(a_1^2+s)(a_2^2+s)(a_3^2+s)}}ds \tag{6}$$

with

$$\frac{y_1^2}{a_1^2+\lambda} + \frac{y_2^2}{a_2^2+\lambda} + \frac{y_3^2}{a_3^2+\lambda} = 1 \tag{7}$$

and

$$\phi = \frac{3}{4}\int_\lambda^\infty \frac{1 - \left(\frac{z_1^2}{a_1^2+s} + \frac{z_2^2}{a_2^2+s} + \frac{z_3^2}{a_3^2+s}\right)}{\sqrt{(a_1^2+s)(a_2^2+s)(a_3^2+s)}}ds \tag{8}$$

with

$$\frac{z_1^2}{a_1^2+\lambda} + \frac{z_2^2}{a_2^2+\lambda} + \frac{z_3^2}{a_3^2+\lambda} = 1. \tag{9}$$

The coordinate transformation for y_i and z_i is defined such that

$$x_1 = y_1 = z_1, \quad x_2 = y_2 = z_2,$$
$$x_3 = y_3 + h = z_3 - h. \tag{10}$$

We have found that the integrals represented by Eqs. (6) and (8), which require the roots of Eqs. (7) and (9), respectively, for λ can be obtained analytically in terms of elementary functions if at least two of the semiaxes a_1, a_2, and a_3 are equal. Accordingly, we have chosen $a_1 = a_2 = 3a_3$ for the example results to be displayed below. The volume of such an inclusion is given by $V = 12\pi a_3^3$. Here, the ellipsoid looks round when viewed from the surface, but its thickness in the x_3 direction may be varied for a basic study of the effect of aspect ratio on the stress field.

As with the point sources discussed in the previous section, the stress field associated with an ordered array of ellipsoidal inclusions may be straightforwardly determined by summing Eq. (5) over all dot positions, in the precise manner as shown for Eq. (3).

C. Cuboidal and trapezoidal inclusions (finite-element method)

The finite element method is best suited to modeling of elastic fields associated with inclusion geometries more complex than ellipsoids. For the creation of the meshes, we used a widely available finite-element analysis software application, ABAQUS. ABAQUS permits the closely controlled generation of finite-element meshes through the use of input files containing complete instructions for node-by-node and element-by-element mesh specification, along with imposition of boundary conditions. For a typical trapezoidal inclusion within a matrix unit cell, elastic solutions may be approximated using a finite-element mesh comprising one quadrant of an arbitrarily deep matrix unit cell, with appropriate boundary conditions imposed at the lateral faces. Meshes generated included one quarter of a cuboidal or trapezoidal inclusion, at various depths, embedded in a matrix of identical elastic properties (see Fig. 4). The mesh uses eight-node linear brick elements with $\mu = 1$ and $\nu = 1/3$. The mismatch strain f was taken as unity by identifying the thermal expansion strain in the inclusion, $\alpha \Delta T$, with unity. In this fashion, any value of f may be considered due to linearity.

Depths of the inclusion centroid varied between $3a_3$ and $12a_3$, for direct comparison with point source and ellipsoidal inclusion results (recall a_3 denotes the half-height of the ellipsoidal inclusion). The FEM domain has lateral dimensions of $6a_3$ in each direction, appropriate for an interinclusion spacing of $12a_3$. For the inclusion shape, truncation angles of 0° and 30° were used (see inset, Fig. 4). The former we refer to as a cuboid, and the latter a trapezoid. The lateral dimension of the inclusion is determined by enforcing that its volume is identical to that of an ellipsoidal inclusion with the same height, $2a_3$. With the volume and thickness fixed, there is an inclusion base dimension associated with each choice of truncation angle α. The inclusions consist of 125 evenly spaced elements, while the matrix elements include a dimensional bias such that they become larger near the far walls, but smaller again as they approach the free surface.

Two general types of cases were investigated. The simplest was the case of a single inclusion submerged in a semi-infinite half space. The second type of case involved an infinite two-dimensional array of submerged inclusions. The
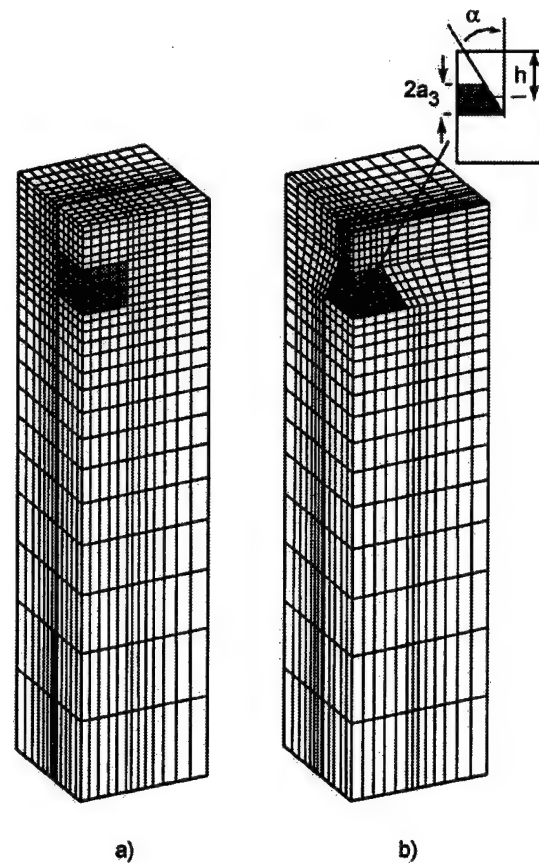

FIG. 4. Mesh used in finite element calculations of elastic fields for (a) cuboidal ($\alpha = 0°$), and (b) trapezoidal ($\alpha = 30°$) quantum dot configurations. One quarter of the domain is needed in this calculation due to fourfold symmetry about the longitudinal axis. The inset shows the critical parameters used to describe the geometry of the quantum dot, including the truncation angle α. The depth h is always taken from the centroid of the quantum dot, and the lateral dimension of the dot is chosen such that its volume is the same as an ellipsoidal dot discussed in Fig. 3.

latter is more difficult to approximate using analytical approaches because of the sum given by Eq. (3). Somewhat surprisingly, however, the periodic case presents fewer obstacles to the finite-element approach than does the singular case.

For models of a single trapezoidal inclusion submerged in a semi-infinite half space, we insist that normal displacement must vanish at the two walls in contact with the inclusion, consistent with the division of the inclusion (and matrix unit cell) into symmetric quadrants.

The bottom surface is constrained similarly, although the type of condition imposed at the bottom is less important than the depth, which should be sufficiently large to be considered "far field." It must be admitted that the use of the same boundary condition as that imposed at the lateral walls in contact with the inclusion does, in fact, give rise to a similar periodicity in depth, which is not intended. However, with a large dimension of matrix below the inclusion, the effect of this depth image stress field will be minimal. We could just as easily use a fully encastered or free boundary condition (or any other that would result in a traction-free far field surface condition), so long as the depth is large and
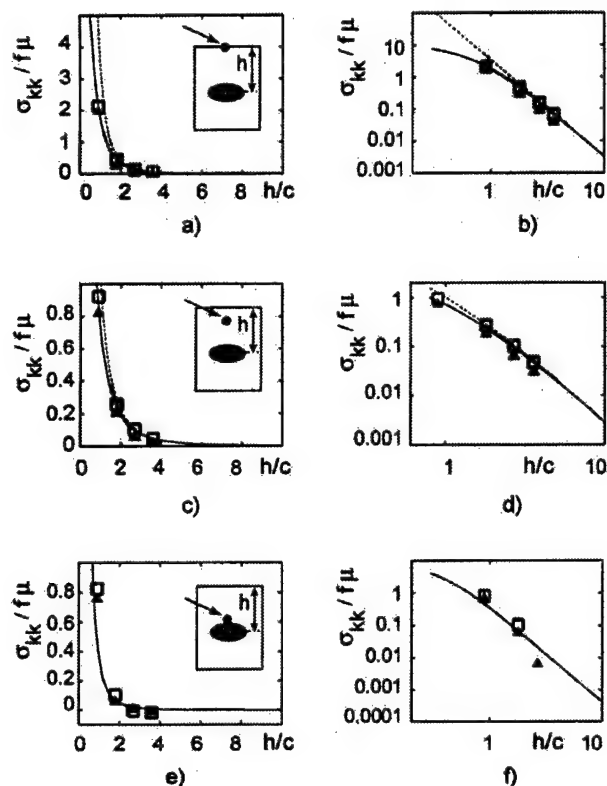
FIG. 5. Plots of stress σ_{kk} versus dot depth, for an isolated dot, for the various models considered in this article. In all cases, the solid line is for an ellipsoidal inclusion ($a_1=a_2=3a_3$); the dashed line is for a point source of dilatation, the open square is for the FEM model of the cuboid, and the closed triangle is for the FEM model of the trapezoidal dot. In (a) and (b) we show the trace of the stress tensor at the surface directly above the dot. In (c) and (d) we show the stress at the surface, evaluated at depth $c/2$ (where c is related to the volume of the dot by $c=V^{1/3}$), above the dot. In (e) and (f) we show the interface stress, that is, the stress evaluated just above the dot/matrix interface. The location of stress evaluation is further indicated in the insets. The figures in the right column [(b), (d), and (f)] use a log-log scale to illustrate the asymptotic dependence of stress on dot depth ($\sigma_{kk}{\sim}h^{-3}$) for large depths.

inclusion volume is small in comparison to the matrix volume. Since the intention is to simulate a semi-infinite domain, the depth of the matrix below the deepest inclusion must be "much larger" than the thickness of the matrix separating the inclusion from the surface. For a finite-element model limited to a relatively small number of elements, this requirement becomes increasingly costly with larger quantum dot submergences. In each case, we make the depth of the overall mesh large enough that there is at least four times more matrix below the base of the inclusion than above it.

The two remaining lateral walls in the mesh for the isolated quantum dot must not reflect a symmetry between groups of four unit cells (to do so would imply an infinite two-dimensional array of submerged inclusions). Rather, we use a condition similar to that used at the bottom surface, that is, we require that the distance between the inclusion and the far lateral walls be large.

For the periodic case, symmetry was enforced with a zero normal displacement condition at all four lateral walls,

so that the elastic field within the mesh is representative of an infinite two dimensional array of submerged inclusions. The zero normal displacement condition results in a mirror image stress field, which if imposed at each lateral wall, appears as the intended inclusion array. Typical meshes included in this investigation contained between 6000 and 10 000 total elements.

IV. RESULTS AND DISCUSSION

A. Single quantum dot

We have seen how stress fields can be obtained for submerged inclusions using the point dilatation model, the misfitted ellipsoid model, or the finite-element cuboid and trapezoid models. Comparison of these fields is undertaken here by evaluation of the trace of the stress tensor (σ_{kk}) at three points of interest: the surface directly above the dot ($x_3=0$), a depth $c/2$ below the surface, where $c\equiv V^{1/3}$, and the upper surface of the dot (at the interface between the dot and the matrix). The latter location is not shown for the point source of dilatation, since the precise interfacial position is not defined. Throughout, Poisson's ratio is taken as 1/3. For the ellipsoid, the aspect ratio is taken as 3, i.e., $a_1=a_2=3a_3$. For the cuboid and the 30° trapezoid, the same height and volume are used as for the ellipsoid.

Figure 5(a) shows the variation of stress at the surface with inclusion depth h. As expected, the stress asymptotically approaches zero as the inclusion is moved further from the surface. The same information is shown on a log-log plot in Fig. 5(b), where it can be seen that the slope of the curves approaches -3, indicative of the $1/h^3$ decay of stress. Moreover, the point source and ellipsoidal stresses converge as the dot exceeds 1.5 to 2 times the cube root of the volume of the ellipse c, which may be regarded as a characteristic length for this stress field. The FEM results are shown as discrete points lying quite close to the ellipsoidal stress curve.

Figures 5(c) and 5(d) show the stress component σ_{kk} at a depth $c/2$ from the surface. Again, good convergence between the ellipsoid and the point source solutions occurs as the depth of the inclusion exceeds $1.5c$ to $2c$. Both sets of finite-element results are in good agreement with the analytic results. The calculated FEM data points in all cases thus far [Figs. 5(a)–5(d)] tend to show slightly more disagreement as the depth of the dot increases. We speculate that this is tied to boundary effects, that is, artificial "image" components exist due to the four lateral faces of the mesh, as well as the bottom surface of the mesh (the latter of which is expected to dominate more for deeper inclusions), which are not manifested in the ellipsoidal or point source solutions.

Finally, in Figs. 5(e) and 5(f), we show the stress just outside of the dot as it is moved from the boundary. Interestingly, this stress component decays to zero. This result, though not intuitive, was first noted by Eshelby[9,10] and does not hold for the other individual stress components at this location. In fact, the stress component σ_{kk} vanishes everywhere outside the ellipsoid (and the point force) in an infinite medium. The image errors mentioned earlier still apply to the FEM data points. In addition, the exact details of the shape of the inclusion should be more important here than in
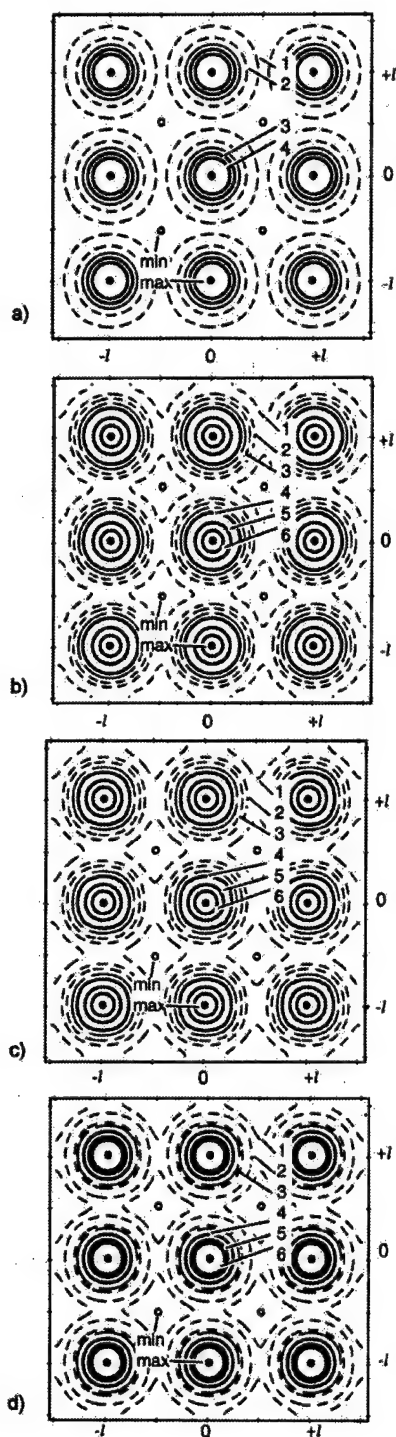
FIG. 6. Contour plots of the trace of the stress tensor at the surface σ_{kk} (in units of $f\mu$), for an array of quantum dots at depth $3a_3$ and spacing ℓ $= 12a_3$. In all cases, positive stresses are denoted by a solid line, negative values are denoted by a dashed line, and a zero value of stress is indicated by the long dashes. (a) Array of point dilatations: values of the nonzero contours are (1) -0.3, (2) -0.2, (3) 0.3, and (4) 0.8, with a minimum of -0.31 and a maximum of 3.3. (b) Array of ellipsoids ($a_1=a_2=3a_3$): values of the nonzero contours are (1) -0.4, (2) -0.3, (3) -0.2, (4) 0.3, (5) 1.0, and (6) 1.5, with a minimum of -0.42 and a maximum of 1.8. (c) Array of cuboids: values of the nonzero contours are (1) -0.38, (2) -0.3, (3) -0.2, (4) 0.3, (5) 1.0, and (6) 1.5, with a minimum of -0.4 and a maximum of 1.9. (d) Array of trapezoids: values of the nonzero contours are (1) -0.29, (2) -0.25, (3) -0.1, (4) 0.3, (5) 0.7, and (6) 1.0, with a minimum of -0.28 and a maximum of 1.9.
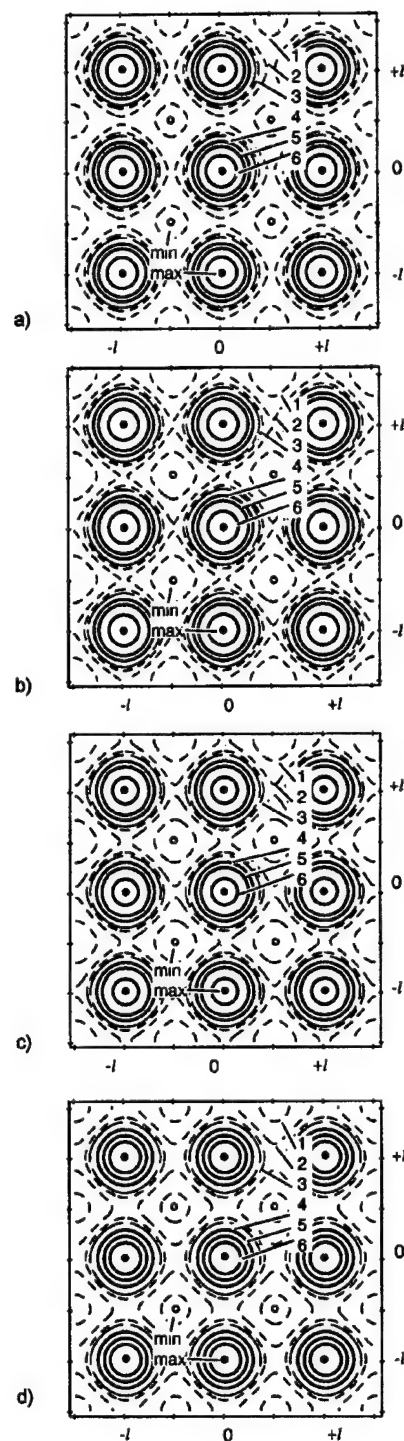
FIG. 7. Contour plots of the trace of the stress tensor at the surface σ_{kk} (in units of $f\mu$), for an array of quantum dots at depth $6a_3$ and spacing ℓ $= 12a_3$. In all cases, positive stresses are denoted by a solid line, negative values are denoted by a dashed line, and a zero value of stress is indicated by the long dashes. (a) Array of point dilatations: values of the nonzero contours are (1) -0.1, (2) -0.05, (3) -0.02, (4) 0.05, (5) 0.1, and (6) 0.2, with a minimum of -0.11 and a maximum of 0.3. (b) Array of ellipsoids ($a_1=a_2=3a_3$): values of the nonzero contours are (1) -0.1, (2) -0.05, (3) -0.02, (4) 0.05, (5) 0.1, and (6) 0.2, with a minimum of -0.14 and a maximum of 0.28. (c) Array of cuboids: values of the nonzero contours are (1) -0.1, (2) -0.05, (3) -0.02, (4) 0.05, (5) 0.1, and (6) 0.2, with a minimum of -0.13 and a maximum of 0.25. (d) Array of trapezoids: values of the nonzero contours are (1) -0.09, (2) -0.05, (3) -0.02, (4) 0.05, (5) 0.1, and (6) 0.15, with a minimum of -0.1 and a maximum of 0.22.
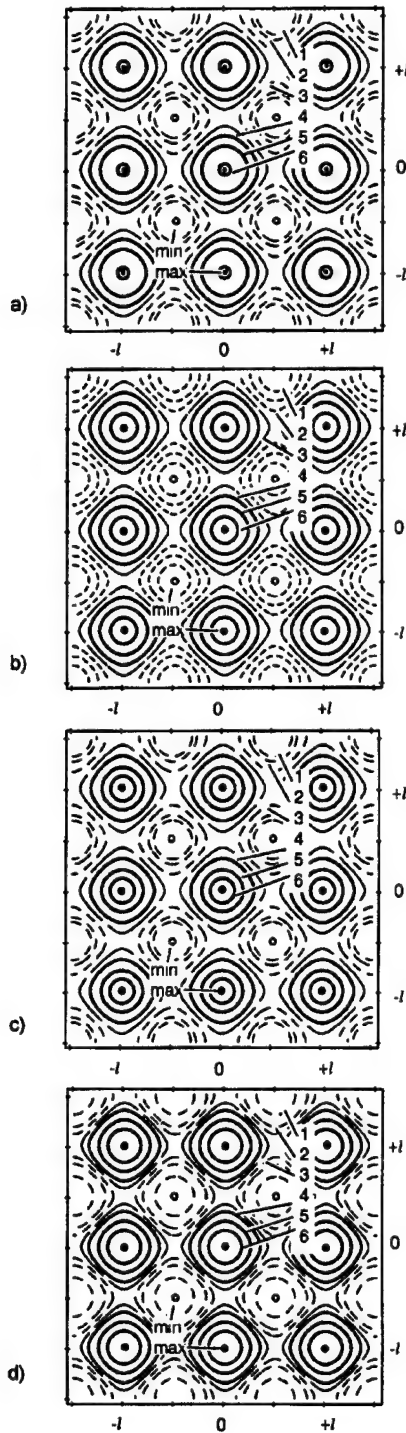
FIG. 8. Contour plots of surface stress σ_{kk} (in units of $f\mu$), for an array of quantum dots at depth $12a_3$ and spacing $\ell = 12a_3$. In all cases, positive stresses are denoted by a solid line, negative values are denoted by a dashed line, and a zero value of stress is indicated by the long dashes. (a) Array of point dilatations: values of the nonzero contours are (1) -0.005, (2) -0.004, (3) -0.002, (4) 0.002, (5) 0.005, and (6) 0.009, with a minimum of -0.0071 and a maximum of 0.0093. (b) Array of ellipsoids ($a_1 = a_2 = 3a_3$): values of the nonzero contours are (1) -0.006, (2) -0.004, (3) -0.002, (4) 0.002, (5) 0.005, and (6) 0.008, with a minimum of -0.0072 and a maximum of 0.0093. (c) Array of cuboids. The values of the nonzero contours are (1) -0.005, (2) -0.004, (3) -0.002, (4) 0.002, (5) 0.005, and (6) 0.007, with a minimum of -0.0066 and a maximum of 0.0083. (d) Array of trapezoids: values of the nonzero contours are (1) -0.004, (2) -0.002, (3) -0.001, (4) 0.001, (5) 0.003, and (6) 0.005, with a minimum of -0.0056 and a maximum of 0.0068.

the earlier cases; therefore, it is not surprising that the trapezoid and cuboid results show a modest level of disagreement with the analytical solution.

B. Ordered array of dots

In this section we consider a square array of dots at various prescribed depths h and spacing $\ell = 12a_3$ [see Fig. 3(b)]. We continue to use the stress trace (σ_{kk}) as a basis for comparison. Specifically, we use surface contour plots of the stress trace predicted by the point dilatation, ellipsoid, and finite-element models. These plots for the trace of the stress tensor at the surface are shown in Figs. 6–8. No evaluation was made of differences between stresses below the surface.

In Figs. 6(a)–6(d) we show stress contours for an array of dots at depth $h = 3a_3$. Specific values denoted by the contours, as well as the maximum and minimum values, are given in the caption in units of $f\mu$. The extrema of the stress distribution appear directly above a given dot, as well as directly above a square quadruplet of four dots. Of all the depths we consider, the dissimilarities between all four results are most evident here, due to the close proximity of the dots to the surface. Moreover, we note the symmetry of the stress distributions due to the point dilatation and the ellipse are of a circular nature, while for the cuboid and trapezoid, the perfect circular symmetry is slightly broken. In other words, the contours reflect the shape of the particular dot. As the dot moves closer to the surface, we expect this feature to become more dominant.

In Fig. 7 the corresponding results are shown for an array of dots at depth $h = 6a_3$. There is moderate quantitative agreement between all four models, indicating that the precise shape of the dot is a much less important factor at this depth. In addition, elements of a square-like symmetry begin to appear in the stress distribution at locations removed from the point directly above any given dot. Moreover, this square-like motif in the stress contours in rotated by 45° with respect to the original square lattice of dots.

Finally, in Fig. 8, the results are shown for an array of dots at depth $h = 12a_3$. A square-like symmetry to the stress distribution (also rotated by 45°), similar to the previous case, is more pervasive. The quantitative level of agreement is good, but not nearly as good as expected for this depth. Several sources of error can be identified that can explain the disagreement: in the FEM results, no image contributions are expected from the lateral walls of the mesh, since the periodic nature of the geometry is perfectly captured. However, the image error from the bottom surface is expected to be most prevalent at this depth than in the earlier cases. In addition, the number of terms needed for the sums in Eq. (3) to obtain good convergence (applicable to the point of dilatation and ellipsoid arrays) became exceedingy large when h is greater than $\sim 10a_3$, and accordingly, we are confident of the results in Figs. 8(a) and 8(b) only to within about $\pm 5\%$.

V. SUMMARY

We conclude that over a wide range of geometries, simple analytical models based on ellipsoids, or to some extent based on point dilatations, may be the most efficient

J. Appl. Phys., Vol. 89, No. 8, 15 April 2001

Romanov *et al.* 4531

means of obtaining reasonable estimates of the elastic stresses associated with quantum dots. In particular, the finite-element models described in this article very closely matched the predictions of the ellipsoidal inclusion model in the isolated and periodic cases. This close correspondence between the analytical ellipsoid and the FEM cuboid/ trapezoid persists to remarkably shallow submergence depths, indicating a potentially high usefulness in modeling typical three-dimensional dot array geometries.

The exception to the close match of ellipsoid and finite-element models is the case of predicted stresses at the upper interface between the dot and the matrix. The interface lies in a region characterized by large stress gradients, which would have an expected detrimental effect on the accuracy of the finite-element models. However, even with an exceptionally fine mesh, differences in modeled dot shape should be expected to give rise to variations in predicted stress values at the interface. These differences would be attributed both to variations in interface depth and to differences in local stress concentrations at the top center interface of dots of different shape.

Of perhaps more use to the modeler of SAQD systems is that only one ''primary'' dot (or region associated therewith) should be considered in detail, while all other dots may be approximated as ellipsoids or point sources.

Finally, we note that the calculations in this article clearly show that quantum dots either on the free surface or near the free surface lead to large hydrostatic stresses and strains in the matrix. The hydrostatic strain will lead to changes in both the conduction and valence band levels. We believe that this effect should be included in the treatment of the matrix electronic properties for near surface dots and stressors.

ACKNOWLEDGMENTS

[1] D. Leonard, K. Pond, and P. Petroff, Phys. Rev. B **50**, 11687 (1994).

[2] A. Zunger, MRS Bull. **23**, 15 (1998).

[3] D. Bimberg, M. Grubdmann, and N. N. Ledentsov, MRS Bull. **23**, 31 (1998).

[4] S. Rouvimov, Z. Liliental-Weber, W. Swider, J. Washburn, E. R. Weber, A. Sasaki, A. Wakahara, Y. Furkawa, T. Abe, and S. Noda, J. Electron. Mater. **27**, 427 (1998).

[5] Q. Xie, A. Madhukar, P. Chen, and N. P. Kobayashi, Phys. Rev. Lett. **75**, 2542 (1995).

[6] V. A. Shchukin, N. N. Ledentsov, P. S. Kop'ev, and D. Bimberg, Phys. Rev. Lett. **75**, 2968 (1995).

[7] J. Tersoff, C. Teichert, and M. G. Lagally, Phys. Rev. Lett. **76**, 1675 (1996).

[8] V. A. Shchukin, D. Bimberg, V. G. Malyshkin, and N. N. Ledentsov, Phys. Rev. B **57**, 12262 (1998).

[9] Y. W. Zhang, S. J. Xu, and C.-H. Chiu, Appl. Phys. Lett. **74**, 1809 (1999).

[10] A. E. Romanov, P. M. Petroff, and J. S. Speck, Appl. Phys. Lett. **74**, 2280 (1999).

[11] H. Lee, J. A. Johnson, J. S. Speck, and P. M. Petroff, J. Vac. Sci. Technol. (to be published).

[12] F. Jónsdóttir and L. B. Freund, Mech. Mater. **20**, 337 (1995).

[13] T. R. Mattsson and H. Metiu, Appl. Phys. Lett. **75**, 926 (1999).

[14] M. Grundmann, O. Stier, and D. Bimberg, Phys. Rev. B **52**, 11969 (1995).

[15] H. Jiang and J. Singh, Physica E (Amsterdam) **2**, 614 (1998).

[16] J. H. Davies, J. Appl. Phys. **84**, 1358 (1998).

[17] J. Groenen, C. Priester, and R. Carles, Phys. Rev. B **60**, 16013 (1999).

[18] J. H. Davies, Appl. Phys. Lett. **75**, 4142 (1999).

[19] J. A. Barker and E. P. O'Reilly, Phys. Rev. B **61**, 13840 (2000).

[20] J. D. Eshelby, Proc. R. Soc. London, Ser. A **241**, 376 (1957).

[21] J. D. Eshelby, Proc. R. Soc. London, Ser. A **252**, 561 (1959).

[22] J. R. Downes, D. A. Faux, and E. P. O'Reilly, J. Appl. Phys. **81**, 6700 (1997).

[23] A. D. Andreev, J. R. Downes, D. A. Faux, and E. P. O'Reilly, J. Appl. Phys. **86**, 297 (1999).

[24] G. S. Pearson and D. A. Faux, J. Appl. Phys. **88**, 730 (2000).

[25] T. Benabbas, P. François, Y. Androussi, and A. Lefebvre, J. Appl. Phys. **80**, 2763 (1996).

[26] A. Ponchet, D. Lacombe, L. Durand, D. Alquier, and J.-M. Cardonna, Appl. Phys. Lett. **72**, 2984 (1998).

[27] T. Benabbas, Y. Androussi, and A. Lefebvre, J. Appl. Phys. **86**, 1945 (1999).

[28] G. Muralidharan, Jpn. J. Appl. Phys., Part 2 **39**, L658 (2000).

[29] W. Yu and A. Madhukar, Phys. Rev. B **79**, 905 (1997).

[30] C. Pryor, J. Kim, L. W. Wang, A. J. Williamson, and A. Zunger, J. Appl. Phys. **83**, 2548 (1998).

[31] M. E. Bachlechner, A. Omeltchenko, A. Nakano, R. K. Kalia, P. Vashishta, I. Ebbsjö, A. Madhukar, and P. Messina, Appl. Phys. Lett. **72**, 1969 (1998).

[32] Y. P. Chiu, J. Appl. Mech. **44**, 587 (1977).

[33] Y. P. Chiu, J. Appl. Mech. **45**, 302 (1978).

[34] T. Mura, *Micromechanics of Defects in Solids* (Martinus Nijhoff, Boston, 1987).

[35] K. Seo and T. Mura, J. Appl. Mech. **46**, 568 (1979).

[36] J. P. Hirth and J. Lothe, *Theory of Dislocations* (Wiley, New York, 1982).

[37] R. De Wit, Solid State Phys. **10**, 249 (1960).

[38] R. D. Mindlin and D. H. Cheng, J. Appl. Phys. **21**, 931 (1950).

[39] J. C. M. Li, Metall. Trans. A **9A**, 1353 (1978).

[40] K. L. Malyshev, M. Yu. Gutkin, A. E. Romanov, A. A. Sitnikova, and L. M. Sorokin, Sov. Phys. Solid State **30**, 1176 (1988).

[41] V. I. Vladimirov, M. Yu. Gutkin, and A. E. Romanov, Mech. Composite Mater. **3**, 450 (1987).

[42] B. Michel, Arch. Mech. **32**, 73 (1980).

[43] F. Loges, B. Michel, and A. Christ, Z. Angew. Math. Mech. **65**, 65 (1985).

Strain-engineered self-assembled semiconductor quantum dot lattices

H. Lee, J. A. Johnson, M. Y. He, J. S. Speck, and P. M. Petroff[a)]
Materials Department, University of California, Santa Barbara, California 93106

We demonstrate a self-assembling method for growing semiconductor quantum dots into ordered lattices. The quantum dot nucleation and positioning into lattices was achieved using a periodic subsurface stressor lattice. Three different two-dimensional -2D! square lattices are demonstrated. The unit cell dimensions, orientation, and the number of quantum dots in the basis are tunable. We find that the 2D lattice can be replicated at periodic intervals along the growth direction to form a three-dimensional -3D! lattice of quantum dots. © *2001 American Institute of Physics.*
DOI: 10.1063/1.1336554#

Semiconductor self-assembled quantum dots -QDs![1-7] provide a convenient means of exploring the physics of zero-dimensional -0D! quantum confined systems. The size of QDs is on the order of the electron wavelength and the carrier energy levels are quantized. The sequential loading of electrons and holes and the 3D confinement character of the carriers in the QDs have been previously demonstrated.[7-9] The sharp density of states in the QDs yields, as expected, ultra narrow luminescence lines and several studies have recently shown the importance and complexity of many-body effects in the relaxation processes involved in strongly excited quantum dots.[10-13] In addition to their "atom-like" properties, the potential application of QDs has been explored in a wide variety of novel devices.[14-18]

Moving from random arrays of "atom-like" QDs to the QD lattice would offer the possibility of novel and unexpected properties which will be tied to the electronic or photonic quantum dot coupling within the array. Ideally, the quantum dot lattice should have long-range order as well as a controllable crystal structure with an adjustable number of QDs in the basis. These ideal properties have not yet been achieved and usually when discussing properties of self-assembled QDs, one deals either with an isolated QD or an ensemble of QDs that are randomly distributed on a plane within a structure. In this case, the electronic coupling is not controlled and is dependent on the QDs density.

In this letter, we discuss a method for self-assembling QDs into periodic lattices using a coherently strained layer deposited by molecular-beam epitaxy over a semiconductor substrate.

Previous attempts to produce spontaneous long-range order in self-assembled QDs using epitaxial deposition may be classified in two categories: -a! prepatterning methods which make use of differences in atomic diffusion on faceted surfaces to control island nucleation[19] and -b! techniques which are using a built-in strain anisotropy introduced on the growing surface.[20-24] The growth of PbSe quantum dots in strain-symmetrized PbSe/Pb$_x$Eu$_{12 x}$Te superlattices[24] is an example of this second category where the spontaneous long range quantum dot ordering into a hexagonal lattice is associated with the strong elastic anisotropy of this material system.

QDs are formed by epitaxial deposition of coherently strained islands and their nucleation is a random process initiated at step edges.[6] The randomness of the nucleation process, even for the case of interacting nuclei growing on an infinitely long and narrow strip of surface, has been demonstrated experimentally[19] and simulated.[25] To minimize the random nucleation, a promising approach appears to nucleate the QDs on a limited surface area such as a mesa top with nanometer dimensions.

To obtain such a periodic lattice of nucleation sites, we make use of surface diffusion on faceted surfaces with a built-in lattice of stressors. We use a periodic strain pattern induced by a coherently strained subsurface stressor layer of In$_x$Ga$_{12 x}$As($x' 0.2$) regrown on a 100 GaAs patterned surface. A square lattice of mesas was patterned on a molecular beam epitaxy -MBE! deposited GaAs film using optical holography on a photoresist film. After the photoresist development and chemical etching in a H$_3$PO$_4$:H$_2$O$_2$:H$_2$O 5 3:1:75 solution, the mesas generated on the surface have a square base with ; 170 nm sides and ; 25 nm height. The 2D mesa square lattice has a periodicity of ; 250 nm along the unit cell primitive vectors. The processed substrates were introduced into the MBE chamber and the oxide layer was thermally desorbed at 630 °C under an As$_2$ flux before 60 nm of GaAs layer was deposited at 600 °C to remove the oxide induced surface damage. An In$_{0.2}$Ga$_{0.8}$As stressor layer and a 10 nm GaAs spacer layer were then deposited at lower substrate temperature -510 °C! to reduce the indium surface migration. The sample temperature was then raised to 530 °C for the deposition of the InAs islands. The island formation was followed by changes of the reflection high-energy electron diffraction pattern and their formation was detected after ; 1.7 ML of InAs deposition. To transform the islands into quantum dots for the photoluminescence measurements, a 10 nm thick top GaAs layer was deposited on top of the islands at 600 °C.

AFM images of three different island lattices formed on top of the mesas are shown in Fig. 1. The three different lattices have unit cells that differ by the orientation of their unit vectors. They were obtained from substrates which were prepatterned with the mesa edges parallel to the ^100& ^110& and 30° off a ^110& direction for the AFM shown in Figs. 1-a!, 1-c!, and 1-b!, respectively. Over 90% of InAs QDs are
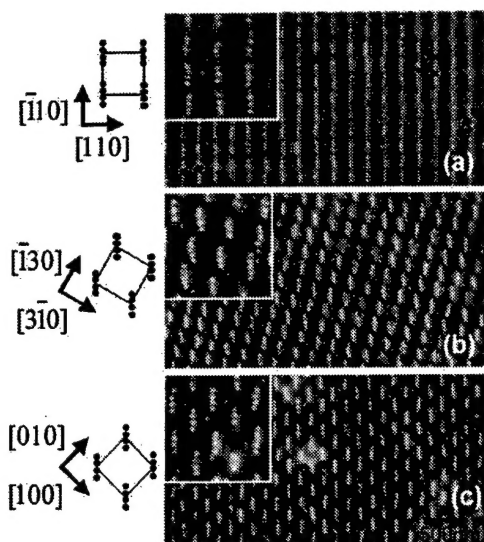
FIG. 1. AFM image of three different island lattices with a square unit cell and a basis of three or four quantum dots aligned along a ⟨110⟩ direction. The vertical direction for all the micrographs is @$1\overline{1}0$#. The unit cell dimensions is 250⨉ 250 nm for all the lattices and the unit cell vectors directions are indicated for the three different lattices in ⟨a⟩, ⟨b⟩, and ⟨c⟩. The insets for each lattice are also shown at higher magnification.
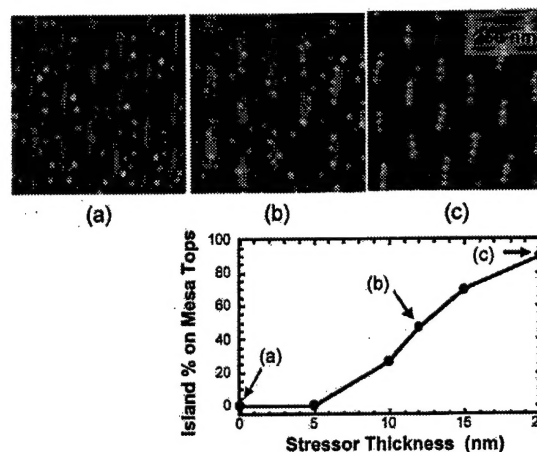

FIG. 2. AFM images of InAs islands distribution for three different stressor layer thicknesses. The graph shows the percentage of InAs islands on top of the mesas as a function of stressor film thickness. The points indicated as ⟨a⟩, ⟨b⟩, and ⟨c⟩ on the graph correspond to the AFM micrographs, respectively. ⟨c⟩ The lattice period is 250 nm and the unit cell sides are aligned along the ⟨100⟩ directions while the basis of the lattice is aligned along a ⟨110⟩ direction.

found on top of mesas for these samples. In all three cases, the lattice periodicity, ; 250 nm, is that of the mesa lattice. The basis of these square lattices contains between three and four islands on average. The islands have diameters ranging from 27 to 45 nm and heights between 4 and 10 nm. When the islands are closely packed on top of the mesas, they appear separated and within the resolution of the AFM with no evidence for coalescence. The density of islands in these lattices is ; 5⨉ 10^9 cm^{-2}. For a nonpatterned sample which was grown simultaneously with the patterned sample, the measured island density was ; 7⨉ 10^9 cm^{-2}. We find that the lattice period is adjustable by changing the mesa lattice period. The number of islands in the basis is controlled through the amount of indium and the mesa size.

We have also successfully grown samples with stacks of QDs lattices of the type shown in Fig. 1⟨c⟩. Cross section transmission electron microscope ⟨TEM⟩ studies of these samples indicate that strain coupling effects[3] between layers of QDs spaced by 10 nm are efficiently propagating the lattice of QDs from one layer to another. The TEM cross section also shows that these 3D QDs lattices are dislocation free.

Since the nucleation of the coherently strained InAs islands takes place as a strain relaxation process, one of the essential elements in controlling their nucleation is the presence of a periodic strain variation on the growth surface. These are formed by combining the mesa with a coherently strained layer below the surface. The nucleation of the InAs islands was compared for stressor film thickness of 0, 5, 10, 12, 15, and 20 nm. The AFM images in Fig. 2 show the InAs islands on patterned substrates for stressor film thickness of 0, 12, and 20 nm. For a structure with a stressor film thickness below 5 nm, all the islands are formed between mesas while for a 20 nm $InO_{0.2}Ga_{0.8}As$ stressor layer nearly all islands nucleate on the mesa tops. In Fig. 2, the island lattice is similar to that shown in Fig. 1⟨c⟩. Similar results were also

observed from regrowth on mesas with different orientations or periodicity. The percentage of InAs islands nucleating on top of the mesas as a function of the stressor layer thickness is also shown in Fig. 2.

To better understand the stressor film effects, the in-plane stress distribution in the different layers is modeled using a finite element elasticity calculation. The in-plane stress is computed using a 1D periodic mesa–valley structure with dimensions similar to the experimental one. A TEM cross section of the mesas and valley profile for an $In_{0.2}Ga_{0.8}As$ ⟨four layers, 5 nm thick⟩/AlAs ⟨three layers, 1 nm thick⟩ stressor film is shown in Fig. 3. The measured height difference between the mesa tops and valleys is ; 5 nm and the width of the mesa tops is ; 20 nm. As a first approximation, the $In_{0.2}Ga_{0.8}As$ stressor film thickness ⟨20 nm⟩ is taken as a constant between the valleys and mesa tops. This assumption is supported by high-resolution TEM cross section measurements that also show that the films are coherently strained with no dislocations. Figure 3 shows a plot of the in-plane stress as a function of position in the InAs wetting layer which is formed on top of the GaAs 100 Å layer prior to the nucleation of the InAs islands. For comparison, Fig. 3 also shows the in-plane stress distribution as a function of position in the wetting layer for a structure which does not contain a stressor layer. The stress data for both curves have been normalized to the stress between a lattice mismatched GaAs and InAs film. The sharp spikes in the stress at the bottom and top of the facet delimiting the mesa edge are related to the finite size of the mesh ⟨also shown in Fig. 3⟩ used for the computation. This simplified model indicates a ; 3%–4% in-plane stress difference between the mesa top and valleys of the wetting layer. The observed preferential nucleation of InAs islands on the mesa tops is consistent with the computed compressive stress distribution for a structure with a sufficiently thick stressor film.

The electronic quality of QD lattices is an important issue for all self-assembling methods that involve a regrowth process.[26] As shown in Fig. 4, the ordered lattice shows a
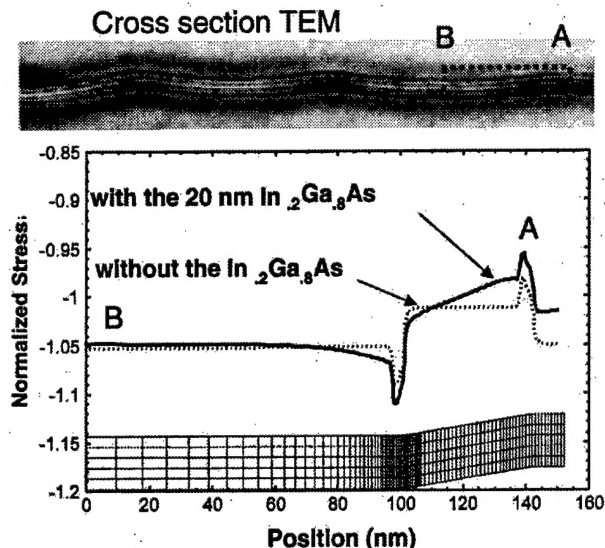
Cross section TEM

FIG. 3. Cross-section TEM image of an $In_{0.2}Ga_{0.8}As$ -four layers, 5 nm thick!/AlAs -three layers, 1 nm thick! stressor film. The AlAs layers have been inserted to underline the mesas and valleys profiles. The @004# dark field imaging conditions are such that the AlAs layers are shown as white layers. A finite element calculation of the in-plane stress distribution for the InAs wetting layer -solid line! is also shown for the areas between A and B on the TEM image. The thin gray line shows the computed stress distribution in the InAs wetting layer for a structure which does not contain the $In_{0.2}Ga_{0.8}As$ stressor layer. The negative values of the normalized stress indicate compressive stresses and the mesh used for the calculation are also shown.

higher photoluminescence -PL! efficiency than the random lattice deposited at the same time. For the QDs lattice, the PL peaks at 1.16, 1.22, and 1.269 eV correspond, respectively, to the ground state and excited states emission. The random QD array shows PL lines at 1.142, 1.203, and 1.269 eV which, respectively, correspond to the ground state and excited states emission. The two spectra have been normalized at the GaAs donor–acceptor pair emission line at ′ 1.51 eV. The higher PL efficiency of the QD lattice is surprising since the QDs density in the lattice (′ 53 10^9 cm^{22}) is about the same as that of the random array. This effect may be related to a higher collection efficiency of the mesa structure. The narrower line widths for the ordered lattice is consistent with
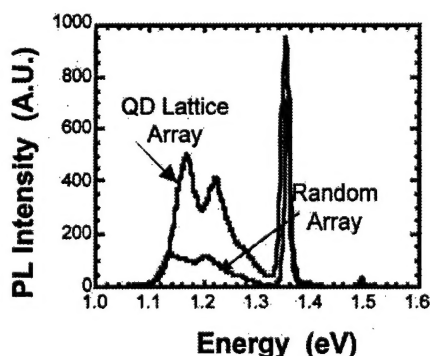

FIG. 4. Photoluminescence spectra at 4.3 K of a 2D QD lattice -dark line! and a random QD ensemble -gray line! of QDs deposited at the same time on an unpatterned substrate. The optical pump power density is 2.5 kW/cm^2.

either reduced size dispersion for the QDs in a lattice and/or electronic coupling of the closely spaced QDs in the crystal basis. In Fig. 4 the PL line at ′ 1.34 eV associated with the $In_{0.2}Ga_{0.8}As$ -four layers, 5 nm thick!/AlAs -three layers, 1 nm thick! stressor layer.

We have demonstrated the controlled formation of two- and three-dimensional QD lattices using a surface strain engineering method. In the present work, we have carried out experiments showing that the lattice period and unit cell structure and size of the 2D lattices are tunable by adjusting the mesa lattice using lithography.

[1] J.-Y. Marzin, J.-M. Gerard, A. Izrel, D. Barrier, and G. Bastard, Phys. Rev. Lett. **73**, 716 -1994!.
[2] D. Leonard, M. Krishnamurthy, C. M. Reaves, S. P. DenBaars, and P. M. Petroff, Appl. Phys. Lett. **63**, 3203 -1993!.
[3] Q. Xie, A. Madhukar, P. Chen, and N. P. Kobayashi, Phys. Rev. Lett. **75**, 2542 -1995!.
[4] K. Georgesson, N. Carlson, L. Samuelson, W. Seifert, and L. R. Wallenberg, Appl. Phys. Lett. **67**, 2981 -1995!.
[5] Y.-W. Mo, D. E. Savage, B. S. Swartzentruber, and M. G. Lagally, Phys. Rev. Lett. **65**, 1020 -1990!.
[6] D. Leonard, K. Pond, and P. M. Petroff, Phys. Rev. B **50**, 11687 -1994!.
[7] N. Kirstaedter, N. N. Ledentsov, M. Grundmann, D. Bimberg, V. M. Ustinov, S. S. Ruvimov, M. V. Maximov, P. S. Kopev, Z. I. Alferov, U. Richter, P. Werner, U. Gosele, and J. Heydenreich, Electron. Lett. **30**, 1416 -1994!.
[8] M. Fricke, A. Lorke, J. P. Kotthaus, G. Medeiros-Ribeiro, and P. M. Petroff, Europhys. Lett. **36**, 197 -1996!.
[9] H. Drexler, D. Leonard, W. Hansen, J. Kotthaus, and P. M. Petroff, Phys. Rev. Lett. **73**, 2252 -1994!; G. Mendeiros-Ribeiro, D. Leonard, and P. M. Petroff, Appl. Phys. Lett. **66**, 1767 -1995!; R. Luyken *et al.*, Appl. Phys. Lett. **74**, 2486 -1999!.
[10] R. J. Warburton, B. T. Miller, C. D. Durr, C. Bödefeld, K. Karrai, J. P. Kothaus, G. Medeiros-Ribeiro, P. M. Petroff, and S. Huant, Phys. Rev. B **58**, 16221 -1998!.
[11] E. Dekel, D. Gershoni, E. Ehrenfreund, D. Spektor, J. M. Garcia, and P. M. Petroff, Phys. Rev. Lett. **80**, 4991 -1998!; F. Findeis, A. Zrenner, M. Markmann, G. Bohm, and G. Abstreiter, Physica E -Amsterdam! **7**, -1999!.
[12] A. Wojs, P. Hawrylak, S. Fafard, and L. Jacak, Physica E -Amsterdam! **2**, 603 -1998!.
[13] M. Grundmann, N. N. Ledentsov, O. Siep, J. Böhrer, D. Bimberg, V. M. Ustinov, P. S. Kop'ev, and Zh. I. Alferov, Phys. Rev. B **53**, 10509 -1996!.
[14] S. Maimon, E. Finkman, G. Bahir, S. E. Schacham, J. M. Garcia, and P. M. Petroff, Appl. Phys. Lett. **73**, 2003 -1998!.
[15] A. Wixforth, J. P. Kotthaus, W. Wegscheider, and M. Bichler, Science **283**, 5406 -1999!.
[16] T. Lundstrom, W. Schoenfeld, H. Lee, and P. M. Petroff, Science **286**, 2312 -1999!.
[17] D. Pan, E. Towe, and S. Kennerly, Appl. Phys. Lett. **73**, 1937 -1998!.
[18] D. G. Deppe and H. Huang, Appl. Phys. Lett. **75**, 3455 -1999!; D. L. Huffaker, G. Park, Z. Zou, O. B. Shchekin, and D. G. Deppe, *ibid.* **73**, 2564 -1998!.
[19] D. S. L. Mui, D. Leonard, L. A. Coldren, and P. M. Petroff, Appl. Phys. Lett. **66**, 1620 -1995!.
[20] G. Jin, J. L. Liu, S. G. Thomas, Y. H. Luo, K. L. Wang, and B.-Y. Nguyen, Appl. Phys. Lett. **75**, 2752 -1999!.
[21] J. Tersoff, C. Teichert, and M. G. Lagally, Phys. Rev. Lett. **76**, 1675 -1996!.
[22] G. Springholz, V. Holy, M. Pinczolits, and G. Bauer, Science **282**, 734 -1998!.
[23] A. Konkar, A. Madhukar, and P. Chen, Appl. Phys. Lett. **72**, 220 -1998!.
[24] G. Jin, J. L. Liu, and K. L. Wang, Appl. Phys. Lett. **76**, 3591 -2000!.
[25] T. T. Ngo, P. M. Petroff, H. Sakaki, and J. L. Merz, Phys. Rev. B **53**, 9618 -1996!; T. T. Ngo and R. S. Williams, Appl. Phys. Lett. **66**, 1906 -1995!.
[26] H. Lee, J. Johnston, J. Speck, and P. M. Petroff, J. Vac. Sci. Technol. B **18**, 2193 -2000!.

REPORT DOCUMENTATION PAGE

Form Approved
OMB No. 0705-0188

1. AGENCY USE ONLY (Leave blank)	2. REPORT DATE 9/4/01	3. REPORT TYPE AND DATES COVERED Final Report 3/15/98-3/14/01

4. TITLE AND SUBTITLE
Periodic Lattices of Interacting Self-Assembled Quantum Dots

5. FUNDING NUMBERS
F49620-98-1-0367

6. AUTHOR(S)
James S. Speck, Pierre M. Petroff, Glenn E. Beltz

7. PERFORMING ORGANIZATION NAME(S) AND ADDRESS(ES)
Materials Department
College of Engineering
University of California
Engineering II
Santa Barbara, CA 93106-5050

3. PERFORMING ORGANIZATION REPORT NUMBER
8-442490-22512

9. SPONSORING/MONITORING AGENCY NAME(S) AND ADDRESS(ES)

Daniel K. Johnstone, Major, USAF
AFOSR/NE
801 North Randolph Street, Room 732
Arlington, VA 22203-1977

10. SPONSORING/MONITORING AGENCY REPORT NUMBER

11. SUPPLEMENTARY NOTES

12A. DISTRIBUTION/AVAILABILITY STATEMENT

12B. DISTRIBUTION CODE

13. ABSTRACT (Maximum 200 words)

Overall, in this program, we developed high quality 2D and 3D periodic quantum dot lattices that show strong photoluminescence. In the initial stages of the program, we worked on QD growth on a periodic stressor lattice formed by ordered subsurface dislocations. The dislocation grid was formed by twist bonding. However, this approach failed because the buffer layer regrowth thickness was too large to a sustain a sufficient strain modulation. We then developed holographic lithography and formed a mesa lattice. In the absence of a stressor, the QDs would typically nucleate in the mesa valleys, not the mesa tops. With the addition of a stressor layer, we demonstrated high quality QD growth on the mesa tops and subsequent stacking of the dots. This work was guided by solid mechanics calculations, careful buffer layer growth studies

In the second year of the program, we have successfully developed a periodic subsurface stressor lattice that has enabled the growth of *ordered* two-dimensional InAs quantum dot arrays. The periodicity of these arrays is controlled by holographic lithography.

14. SUBJECT TERMS
Self-Assembled Quantum Dots,

15. NUMBER OF PAGES
23

16. PRICE CODE

17. SECURITY CLASSIFICATION OF REPORT	18. SECURITY CLASSIFICATION OF THIS PAGE	19. SECURITY CLASSIFICATION OF ABSTRACT	20. LIMITATION OF ABSTRACT
Unclassified	Unclassified	Unclassified	